Application of Fast Optical Tomography to Flow Tubes

Prepared by

E. J. BEITING
Aerophysics Laboratory

15 February 1989

Prepared for

VICE PRESIDENT
Laboratory Operations

Laboratory Operations
THE AEROSPACE CORPORATION

19981118 116

AG499-02-0023

LABORATORY OPERATIONS

The Aerospace Corporation functions as an "architect-engineer" for national security projects, specializing in advanced military space systems. Providing research support, the corporation's Laboratory Operations conducts experimental and theoretical investigations that focus on the application of scientific and technical advances to such systems. Vital to the success of these investigations is the technical staff's wide-ranging expertise and its ability to stay current with new developments. This expertise is enhanced by a research program aimed at dealing with the many problems associated with rapidly evolving space systems. Contributing their capabilities to the research effort are these individual laboratories:

Aerophysics Laboratory: Launch vehicle and reentry fluid mechanics, heat transfer and flight dynamics; chemical and electric propulsion, propellant chemistry, chemical dynamics, environmental chemistry, trace detection; spacecraft structural mechanics, contamination, thermal and structural control; high temperature thermomechanics, gas kinetics and radiation; cw and pulsed chemical and excimer laser development including chemical kinetics, spectroscopy, optical resonators, beam control, atmospheric propagation, laser effects and countermeasures.

Chemistry and Physics Laboratory: Atmospheric chemical reactions, atmospheric optics, light scattering, state-specific chemical reactions and radiative signatures of missile plumes, sensor out-of-field-of-view rejection, applied laser spectroscopy, laser chemistry, laser optoelectronics, solar cell physics, battery electrochemistry, space vacuum and radiation effects on materials, lubrication and surface phenomena, thermionic emission, photosensitive materials and detectors, atomic frequency standards, and environmental chemistry.

Computer Science Laboratory: Program verification, program translation, performance-sensitive system design, distributed architectures for spaceborne computers, fault-tolerant computer systems, artificial intelligence, microelectronics applications, communication protocols, and computer security.

Electronics Research Laboratory: Microelectronics, solid-state device physics, compound semiconductors, radiation hardening; electro-optics, quantum electronics, solid-state lasers, optical propagation and communications; microwave semiconductor devices, microwave/millimeter wave measurements, diagnostics and radiometry, microwave/millimeter wave thermionic devices; atomic time and frequency standards; antennas, rf systems, electromagnetic propagation phenomena, space communication systems.

Materials Sciences Laboratory: Development of new materials: metals, alloys, ceramics, polymers and their composites, and new forms of carbon; nondestructive evaluation, component failure analysis and reliability; fracture mechanics and stress corrosion; analysis and evaluation of materials at cryogenic and elevated temperatures as well as in space and enemy-induced environments.

Space Sciences Laboratory: Magnetospheric, auroral and cosmic ray physics, wave-particle interactions, magnetospheric plasma waves; atmospheric and ionospheric physics, density and composition of the upper atmosphere, remote sensing using atmospheric radiation; solar physics, infrared astronomy, infrared signature analysis; effects of solar activity, magnetic storms and nuclear explosions on the earth's atmosphere, ionosphere and magnetosphere; effects of electromagnetic and particulate radiations on space systems; space instrumentation.

APPLICATION OF FAST OPTICAL TOMOGRAPHY TO FLOW TUBES

Prepared by

E. J. Beiting
Aerophysics Laboratory

15 February 1989

Laboratory Operations
THE AEROSPACE CORPORATION
El Segundo, Calif. 90245

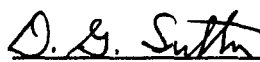Prepared for
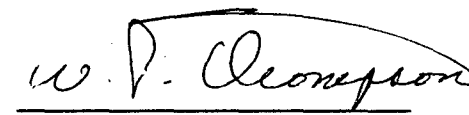
VICE PRESIDENT
Laboratory Operations

APPLICATION OF FAST OPTICAL
TOMOGRAPHY TO FLOW TUBES

Prepared

E. J. Beiting

Approved

D. G. Sutton, Head
Propulsion and Environmental
Sciences Department

W. P. Thompson, Director
Aerophysics Laboratory

ABSTRACT

In this report, the requirements are considered for a two-dimensional flow visualization diagnostic capable of nonintrusively measuring temperature and species concentration in a turbulent, atmospheric pressure flow tube. The need for and the history of flow visualization techniques are briefly reviewed. A new approach is then suggested, based on optical tomography, that would have several advantages over methods currently under development. An up-to-date reference list for optical tomography is included. The feasibility studies completed to date are presented in the bulk of the report.

ACKNOWLEDGMENT

CONTENTS

FIGURES

TABLES

I. INTRODUCTION

A. BACKGROUND

Current research in reacting and nonreacting flows is motivated by a
desire to understand basic processes and specific practical devices. For
nonreacting flows, applications to sonic systems include aerodynamics of
fixed and rotating airfoils, gas turbines, and turbulent mixing problems.
High-pressure nozzles, rocket propulsion (chemical and electric), and shock
waves are supersonic nonreactive flows of interest. Reactive flows can be
classified as steady state or turbulent. Steady-state flows often studied
are stabilized premixed and diffusion flames, and laminar flow reactors and
incinerators. Examples of turbulent reacting flows, however, are consider-
ably more numerous and of greater practical importance. These include
nearly all commercial combustors used for power generation and operated
with fossil fuels; coal gasifiers; internal combustion engines; open cycle
magnetic hydrodynamic (MHD) power generators; and the study of propulsion
systems (gas turbine, ramjet, afterburner, and rocket). To understand
turbulent reacting flows, hydrodynamics and spatially specific chemical
kinetics must be understood in order to quantitatively model the system.

A system problem of immediate interest to the Air Force Space Division
(AFSD) is the disposal of hydrazine by incineration. Of particular inter-
est is the rate of competitive chemical reactions involved in the combus-
tion of N_2H_4, which is very sensitive to temperature. This temperature
sensitivity and the dependency of the final products (specifically, NO_x
pollutants) on the flow contours in the mixing process require a detailed
understanding of the relationship among the macroscopic flow parameters,
temperature, and chemical kinetics. Computer models are often used to
further this understanding. However, these models require the solution of
the conservation equations of continuity and momentum, and a scalar (tem-
perature or concentration) for a high-turbulence Reynolds number in a den-
sity-weighted (Favre-averaged) form. Solution of these equations often
involves making empirical, unjustifiable, or even erroneous assumptions.

1

For example, turbulence chemistry closure requires a probability density function that is chosen somewhat arbitrarily; the turbulent transport process is often cast in the form of a turbulent eddy diffusivity, a concept increasingly under attack; and finally, the modeling of dissipation terms is empirical, at best (Ref. 1). These assumptions require that a considerable database be collected on systems of practical importance before models are implemented.

The history of the diagnostic techniques used to probe hostile flows parallels that of scientific apparatus in general. Originally, intrusive probes were used to sample gas streams (thermocouples, Pitot tubes, and devices to extract and route samples to on-line chemical analyzers). These devices were slow, limited to relatively benign environments, and more importantly, often perturbed the parameter being measured. Optical techniques did not have these problems, and they proliferated with the advent of the laser. Line-of-sight techniques (sodium line reversal, absorption spectroscopy, and one- and two-color laser transmissometry for particle-ladened flows) were the first optical techniques to be implemented. As technology improved, spatially precise (point) measurements could be made using laser-induced fluorescence (LIF), spontaneous Raman scattering (SRS), Rayleigh scattering (RS), coherent anti-Stokes Raman scattering (CARS), laser Doppler velocimetry (LDV), and Mie scattering (MS). Further sophistication led to simultaneous measurements of points along a line for LIF, SRS, and RS (and marginally for CARS).

If photographic techniques are neglected, the field of flow visualization began when technology developed enough to allow the two-dimensional implementations of some of the preceding processes. The relative strengths of these processes are compared in Table 1. This table reveals that the principal disadvantage of SRS and RS is their lack of strength. Several planar Raman scattering experiments have been attempted (Refs. 2-5). Because of the exceedingly small scattering cross sections of Raman scattering, these experiments usually employ multipass cells relaying a high-intensity laser beam through a small measurement area in a nonluminous

2

Table 1. Cross Sections for Various Physical Processes

Physical Process	Differential Cross Section (cm^2/sr)
Particle Scattering (Mie)	
10 µm diam	10^{-7}
0.1 µm diam	10^{-13}
Atomic Fluorescence	
Strong, Visible	$10^{-13} - 10^{-18}$
Molecular Fluorescence	
Simple Molecules	$10^{-19} - 10^{-24}$
Rayleigh Scattering	
N_2, 532 nm	7×10^{-28}
Rotational Raman Scattering	
N_2, all Lines, 532 nm	7×10^{-30}
N_2, Strong Line (Including Population Factor), 532 nm	3.5×10^{-31}
Vibrational Raman Scattering	
N_2, Stokes Q-Branch, 532 nm	3×10^{-31}

environment. Because the Raman signal can be overwhelmed easily by emission, RS is limited to the most benign laboratory environments. Planar Mie scattering (Refs. 6-9) and Rayleigh scattering (Ref. 10) have been used to measure temperature or composite density fields in atmospheric pressure flows. MS requires that the flow be seeded with particles. Inferring temperature or density from these data requires many assumptions (e.g., constant pressure, homogeneous optical characteristics of the gas mixture, uniform particle seeding, and uniform particle size) that restrict these techniques to carefully controlled environments. Additionally, neither MS nor RS can differentiate among chemical species. Despite these shortcomings, interest in these techniques continues, because the higher signal strengths allow the plane of radiation to be translated quickly through the flow, permitting an electronic camera to record a sequence of planar images that may be later reconstructed into a three-dimensional view (Refs. 8-10).

Most recent work in flow visualization has employed planar LIF because of its strong scattering cross section and because it is species specific. Hanson's group at Stanford has been most actively developing this technique. We reference only a few of his recent publications (Refs. 11-15). Hanson has recently extended this technique to include two-photon absorption (Refs. 13, 14) and a three-dimensional image of flow fields (Ref. 15).

Despite these successes, LIF has two drawbacks. First, it requires optical access outside the plane being studied. Second, and more serious, is collisional quenching of the laser excited state. Quenching is a large effect that greatly hinders the quantitative interpretation of the data, thus limiting the use of this technique to extremely well-characterized environments. (Quenching coefficients are sensitive to temperature and to the relative concentrations of surrounding species.) In poorly characterized environments, the data are only useful for study of turbulent structures.

B. MULTIANGULAR ABSORPTION AND TOMOGRAPHIC RECONSTRUCTION

Simple optical absorption was one of the earliest optical diagnostic techniques applied to gas flows but has received scant attention in recent years because of its lack of spatial specificity. Nevertheless, this technique has several highly desirable attributes: its cross section is large --the same as that for LIF; quenching is not a problem; its data are straightforward to interpret; it is species specific; and it can be used to measure concentrations and/or temperature. The principle of optical absorption is based on Beer's law

$$-\ln(I/I_o) = \int_o^L n_i(T)q_i(\nu)d\ell$$

where I_o (I) is the intensity of light before (after) it traverses the sample, $n_i(T)$ is the number density of species i at temperature T, $q_i(\nu)$ is the absorption cross section at frequency ν, and L is the path length over which absorption occurs. For low concentrations, this expression can be linearized

$$(I - I_o)/I_o = \int_o^L n_i(T)q(\nu)d\ell$$

The dynamic range of optical absorption can be expanded by viewing two spectral lines simultaneously. The strengths of the absorption cross sections of these two lines are chosen to differ by an order of magnitude (see Section V.B).

The principal disadvantage of absorption measurements--the lack of site specificity--can be eliminated by making a series of measurements at a number of different angles. This collection of measurements then can be used to mathematically construct a cross-sectional view of the flow (Fig. 1a). This procedure is the principle underlying the well known computerized axial tomography (CAT) scanners used for medical diagnostics. The essence of the procedure can be understood with the aid of Fig. 1. The problem consists of recovering a two-dimensional function F(x,y) from a series of projections P(r,θ) that are related to the absorption as

5

$$P(r,\theta) = \int_{-\infty}^{+\infty} F(x,y)\, ds$$

$$= -\ln\left[I(r,\theta)/I_0\right] \qquad \text{(a)}$$
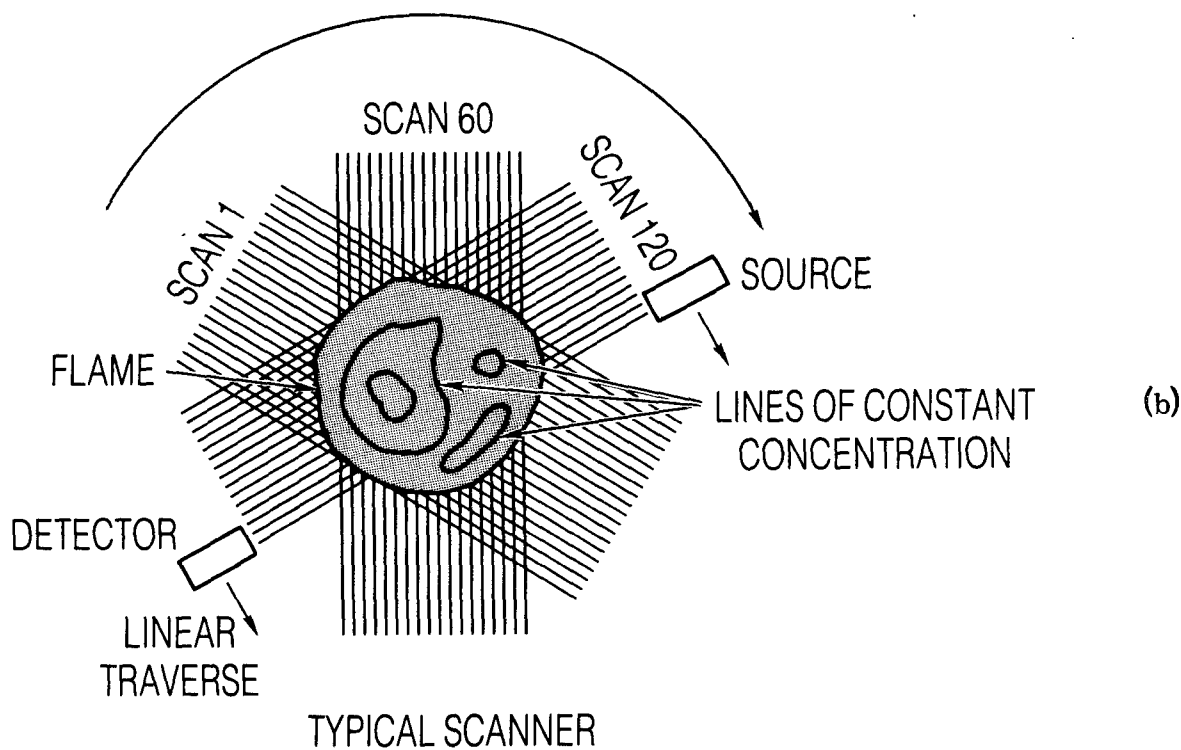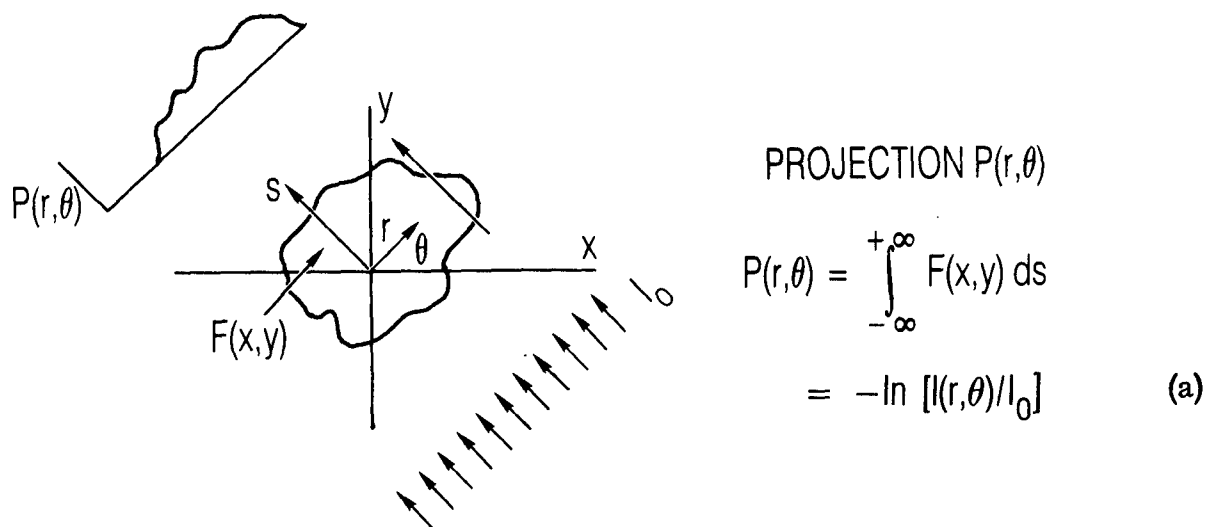
Fig. 1   (a) Geometrical and Mathematical Relationships Between Projection
         P(r,θ) and Cross-Sectional Rays F(x,y) in Tomography; (b) Geom-
         etry of a Typical Scanning Parallel Beam Tomographic Instrument
         (from Ref. 20).

$$P(r,\theta) = \int_{-\infty}^{\infty} F(r,s)ds$$

$$= \int_{-\infty}^{\infty} N_i q_i ds = -\ell n(I/I_o)\big|_{r,\theta}$$

The rays traversing the probed region need not be parallel. A fan beam geometry (Fig. 2) is often used in commercial medical CAT scanners because it usually results in shorter data acquisition times.

Inversion algorithms to obtain $F(x,y)$ from the experimentally measured $P(r,\theta)$ are generally classified as either Fourier transform or linear superposition. In the former, the one-dimensional Fourier transform of the projection is taken to obtain the spatial spectrum $\underline{P}(\omega,\theta)$:

$$\underline{P}(\omega,\theta) = \int_{-\infty}^{\infty} P(r,\theta)e^{-i\omega r}dr = \int_{-\infty}^{\infty}\int_{-\infty}^{\infty} F(r,s)e^{-i\omega r}drds$$

This spatial spectrum can be written as a two-dimensional Fourier transform using the "central slice theorem"

$$\underline{P}(\omega,\theta) = \int_{-\infty}^{\infty}\int_{-\infty}^{\infty} F(r,s)\exp[-i(\phi r + \eta s)]drds\big|_{\eta = 0}$$

This integral is evaluated along the line $\eta = 0$ in the two-dimensional frequency plane. The spatial frequency is given by ρ and $\omega = 2\pi\rho$. A continuous sweep of 180° (360° for fan beam geometry) is required to define $\underline{P}(\omega,\theta)$. The desired function $F(x,y)$ is obtained as the inverse Fourier transform of $\underline{P}(\omega,\theta)$, which, in turn, is obtained experimentally from $P(r,\theta)$. This procedure can be implemented quickly using fast Fourier transform techniques (Refs. 16, 17), but a "back projection" algorithm has been developed (Ref. 18) that is considerably faster, allows the use of filter functions for smoothing, and is stable when $P(r,\theta)$ is inferred from noisy data.
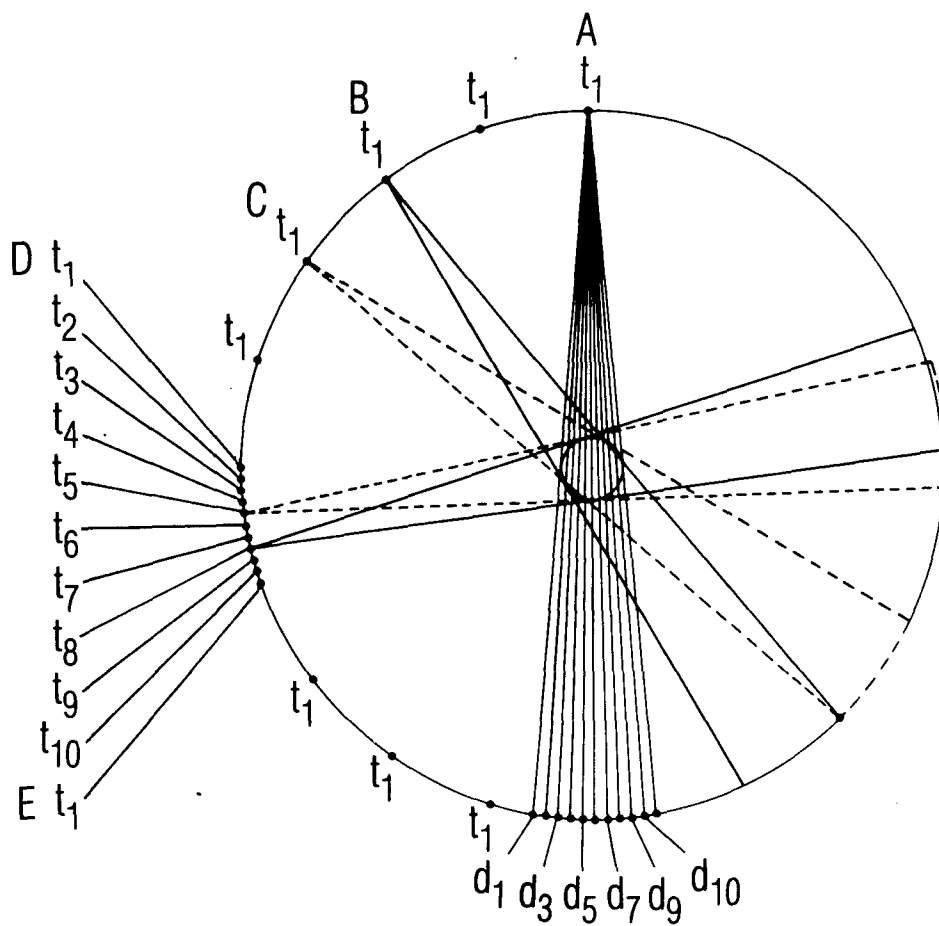
Fig. 2. Geometry of the Time-Multiplexed Fan Beam Tomography Instrument Introduced in the Text

Linear superposition techniques are based upon algorithms that repeatedly adjust the estimated F(x,y) map until convergence is attained. An example of this procedure is the algebraic reconstruction technique (ART), which divides the (x,y) plane into a grid of elements that further divide each beam (r,θ) into a set of i segments of known weight s_i

$$P(r,\theta) = \sum_i s_i(x,y) \, F_i(x,y)$$

Iterative methods have been used to solve systems of 200 × 200 equations for this application (Ref. 19).

Optical tomography was first suggested for the study of reacting flows in 1980 by Goulard and Emmerman (Ref. 20). However, given the importance of the problems that optical tomography can potentially solve, experimental implementation of the technique has been slow. Goulard and Ray (Ref. 21), and Ray and Semerjian (Ref. 22) have described experiments undertaken at NBS. In these experiments, temperature and concentration fields were measured in a symmetric, steady-state, premixed methane/oxygen/diluent flame using OH as the probed species. Narrow frequency light produced by a continuous-wave (cw) ring dye laser was scanned through an absorption line of OH (see Fig. 1b). A rotating mirror geometry swept the beam through the burner, creating a projection in 1 ms at a single wavelength. Scanning could not be done at more than a single projection angle; therefore, cylindrical symmetry was assumed to perform the reconstruction. Absorption experiments also have been undertaken at Stanford University by Byer and his students (Refs. 23-25). They used a fan beam geometry and rotating mirror to create reconstructions of cold flowing I_2 at 90 to 360 angles on 90 detectors using a cw Ar^+ laser. This procedure allowed data to be acquired for reconstruction of concentrations in 100 ms. The data aquisition times of this method can be reduced by at least an order of magnitude. Recently, Synder and Hesselink (Ref. 26) demonstrated a novel configuration using holographic optical elements and a rotating mirror. In this proof-of-principle work, only one angle was measured, and the solid

sample was spun to create the multiple projection angles. Variations in the index of refraction can be used to measure density, and, indirectly, temperature fields using beam deflection tomography (Refs. 27-30) or interferometric tomography (Refs. 31-34). All the work cited in References 27-33 used rotating mechanical elements and cw lasers, thus restricting the measurements to the millisecond time scale. This time scale is too long to freeze turbulent cells in unsteady flows. Recently, however, a fast (300 μs) interferometric tomographic image was recorded on a cylindrically shaped piece of film (Ref. 34). This demonstration was the first instantaneous optical tomographic reconstruction of a nonstationary fluid flow. Several implementations of optical emission tomography have recently been demonstrated (Refs. 35, 36). Reviews of optical tomography for applications to fluid flows are now available (Refs. 37, 38). [Also, see the issue of Applied Optics devoted to computer tomography (Ref. 39).]

C.   PROPOSED INSTRUMENT DESIGN

A novel optical instrument for tomographic studies of turbulent, reacting gas streams is briefly described in this subsection. This instrument differs substantially from those used previously in experimental demonstrations of fluid flow tomography. It produces higher resolution (100 angles, 100 detectors/angle) images; has faster response, thereby effectively freezing the flow (10^{-7} vs 10^{-2}s); uses pulsed rather than cw radiation; and has no moving parts. Furthermore, the instrument is easily scalable, through its unique time-multiplexing design, to higher resolution, greater dynamic range, multispecies detection, or even to a configuration that allows the temporal development of turbulent structure to be viewed through a series of fast snapshots.

Figure 2 illustrates the geometry of the proposed instrument. The center circle represents the cross section of the flow to be investigated. The circumference of the outer circle describes a locus of point sources, each of which consists of a diverging beam of light described by a fan. The rays from each source (point A in Fig. 2) pass through the probed

10

region and terminate on a series of detectors (d_1-d_{10}) also located on the outer circle. If the sources are well separated (points B and C), rays from their fans will not overlap on the opposite side of the circle, and a one-to-n correspondence will exist between the sources and detectors, where n is the number of detectors in each fan. Figure 2 depicts a geometry where 10 nonoverlapping sources could be placed on a 180° semicircle. If 100 detectors were placed in each fan, a moderate resolution tomographic reconstruction of a flow could be performed.

Now, consider placing nine additional sources between sources D and E, as shown. Further, consider that these sources are activated sequentially so that source t_1 is emitting a fan of radiation at time t_1, source t_2 is emitting a fan of radiation at time t_2, etc., and that the time interval between each pulse of radiation is greater than the time any source is active. Then, a detector will receive the radiation from only one source at a time. A train of these radiation pulses can be created from a single output pulse of a tunable laser by relaying the pulse back and forth 10 times between two retroreflectors, laterally displacing it at a fixed distance on each pass. A partially reflecting mirror inserted at 45° into this ladder of parallel paths will cause a portion of the pulse to be directed by the beam splitter through a lens and focused into a bundle of 10 optical fibers on the first pass through this system. These 10 fibers carry their simultaneous pulses to the 10 locations marked t_1 on the circumference of the outer circle. The next pass through the beam splitter creates another pulse at t_2, which is relayed to the 10 locations on the outer circle adjacent to t_1. In this way, 100 sources are created, but only 10 widely separated sources are active at any instant. In this example, each source illuminates 100 detectors, creating 100 angle × 100 detector resolution with only 1000 detectors. Through the multiple use of each detector, a larger detector size is possible for a given spatial resolution. This allows the acquisition of data with a higher signal-to-noise ratio.

11

Note the versatility of this time-multiplexed design. By the introduction of a second sequence of pulses into the fiber at a different wavelength, a second spectral line can be probed, allowing both the temperature and the concentration of the species to be measured. A third sequence of pulses allows the concentration of another species to be measured, etc. Or, the second sequence of pulses can be used to obtain a second "snapshot" of the same species at a later time, thus tracing the time evolution of the flow. Multiple snapshots can then be used to create a minimovie. Currently, an integrated circuit is available that allows the sampling of a train of 640 pulses at time intervals of 10 ns or longer.[*] These 640 pulses can enhance resolution, sample multiple species, or acquire a fast series of images.

The necessary time resolution of the instrument is determined by the requirement to "freeze" a resolution element. The resolution element should approach the smallest space scale of the turbulence. For flow velocities not much greater than 100 m/sec, the smallest space scale, or eddy, will be approximately 1 mm (Ref. 40). If an element is considered to be frozen when it does not move more than 10% of its size, all data must be collected in 10^{-6} sec. As the velocity decreases and the scale size increases, the time resolution of the instrument can be relaxed considerably.

There are three areas of preliminary work that must be completed before a prototype can be built: (1) analytic studies to test the application of this concept to a transparent tube of turbulent gas; (2) software development for the tomographic reconstruction algorithms; and (3) laboratory studies to develop components of a prototype system. The remainder of this report presents results from the first area of preliminary work.

---

[*]LeCroy, monolithic model MVV200, 320/640-cell analog shift register, LeCroy Research Systems Corporation.

II. GEOMETRICAL CONSIDERATIONS

A. PLANAR GEOMETRY

As noted in Section I.B, tomography may be implemented either with a parallel beam or a fan beam geometry. The concept introduced in Section I.C is intrinsically a fan beam design. Artifacts introduced from the reconstruction of fan beam projections limit the allowable geometries, as do considerations of detector size, laser speckle noise, minimum size of turbulence cells, etc. Accordingly, we begin analysis by deriving a number of useful relations among the system variables for a planar fan beam geometry intercepting a cylindrical flow.

Consider the geometry shown in Fig. 3. A fan beam of full angle θ emanates from point B, located on a source-detector circle of radius R, and passes through an inner concentric circle of radius r, which represents the cross section of the flow to be interrogated. The edges of the fan are tangent to the flow cross section and strike the source-detector ring at points C and D, defining an arc of length s. The arc s subtends an angle ϕ with the common center point A. Noting

$$\beta - \frac{\theta}{2} = \alpha$$

$$2\alpha + \phi = \pi$$

$$2\beta + \theta = \pi$$

and eliminating α and β, we find

$$\phi = 2\theta \tag{1}$$

The cosine law for triangles BCD and ACD yields, respectively

$$c^2 = 8a^2 (1 - \cos\theta) \tag{2}$$

$$c^2 = 2R^2 (1 - \cos\phi) \tag{3}$$

13
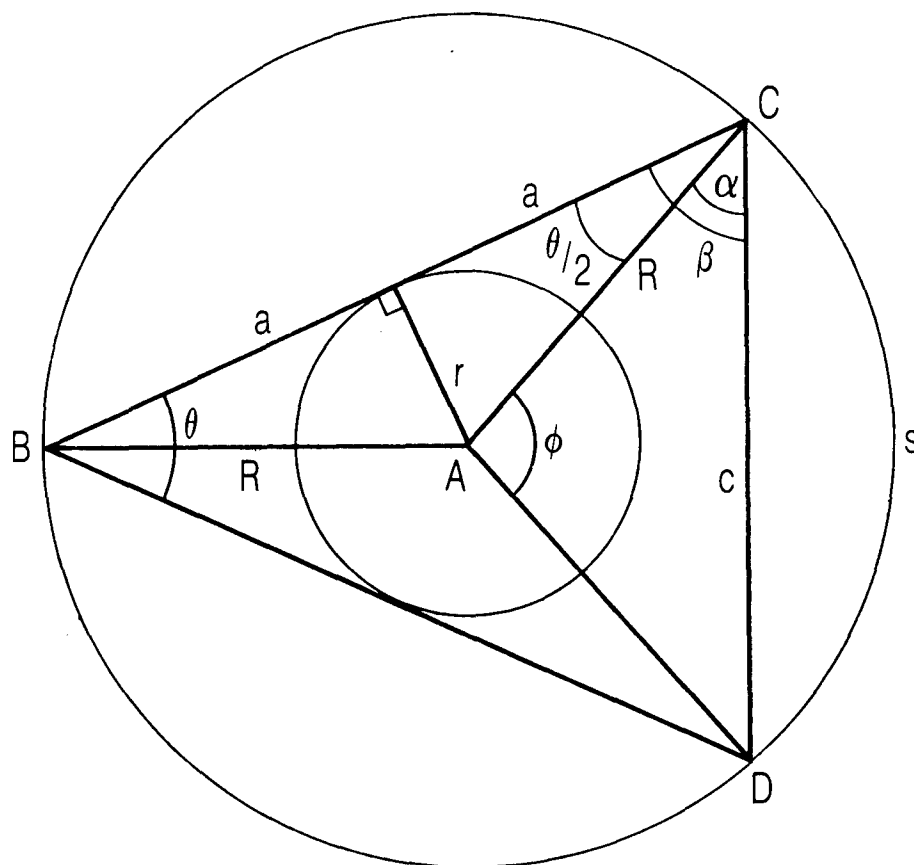
Fig. 3. Geometry Used to Calculate the Optimum Planar Fan Beam Configuration

Solving Eqs. (1-3) for $\phi(r,R)$ and noting $\phi = s/R$, we find the relationship between the arc length and the two radii

$$s = 2R \cos^{-1}\left(1 - \frac{2r^2}{R^2}\right) \tag{4}$$

If w is the width available for each detector, N_d is the total number of detectors, N_f is the total number of fibers, F_m is the multiplexing factor, n_d is the number of detectors per fiber, and N_a is the number of arcs per circumference, then

$$2\pi R = N_d w = N_a s \tag{5}$$

and

$$N_d = n_d N_f / F_m = N_a n_d \tag{6}$$

Combining Eqs. (4-6), we have

$$R = \left\{2/\left[1 - \cos(\pi/N_a)\right]\right\}^{1/2} r = Fr \tag{7}$$

$$w = \frac{2\pi Fr}{N_a n_d} \tag{8}$$

$$F_m = N_f / N_a \tag{9}$$

where F is the ratio of the diameter of the source-detector ring to the diameter of the flow, and the multiplexing factor F_m is the number of times each detector is used in one reconstruction data set. Multiplexing allows for a lower total number of detectors and a smaller source-ring diameter for a given resolution. For large N_a, the factor F scales as N_a, indicating that w scales as r/n_d, independent of N_a and the multiplexing factor. That is, for a given resolution (n_d, N_f), the detector size is dictated solely by the flow diameter. This constraint can be relaxed if the source-ring radius is not equal to the detector-ring radius (nonplanar geometry), as discussed in the next subsection.

15

Equations (6)-(9) can be used to select an appropriate fan beam geometry for interrogating a cylindrical flow, subject to the following guidelines. Since complexity and cost of the proposed tomographic instrument are directly proportional to the total number of detectors, but the resolution is proportional to the product of the number of fibers and the number of detectors per fiber, n_d should be as large as possible, and N_d, as small as possible. This implies a large factor F_m, which in turn requires a small N_a. N_a, however, cannot be made too small, as the practical limit for the fan angle lies between 45 and 60°. For a given flow diameter, a compact instrument requires a small source-detector ring diameter requiring a small value of F. There are two other reasons for keeping R small. First, coherent (laser) radiation passing through a multimode, step-index fiber forms a speckle pattern on the detector surfaces. This random pattern is a source of noise; therefore, the grain size of this speckle should be kept small compared to the detector dimensions. The grain size increases as the separation between the fiber and detector increases. Second, beam displacement at the detector surface, resulting from turbulence-induced index of refraction fluctuations and temperature gradients within the flow, increases with the separation between the absorbing element and detector. Reconstruction artifacts also place constraints on the geometry. For example, interpolation error is introduced if imaging is attempted at radii less than 0.5 R, restricting F to values greater than 2 (Ref. 23). Conversely, the detector size should be kept as large as possible (implying a large R) to keep the preceding effects small compared to the detector dimensions. Of course, the larger the R, the larger n_d can be for a given detector width w. Thus, the ideal design is to have large area detectors on a small (but not too small) ring diameter.

Finally, for the commonly employed mathematical expression used for the fan beam geometry in the convolution back projection algorithm [the Ramachandran-Lakshmunarayanan (R-L) kernel (Ref. 18)], spatial resolution at the center of the reconstructed image is approximately one-half the detector spacing when $N_f \approx n_d$ (Ref. 23). This rule of thumb allows an approximate number of pixels to be assigned to a given fan beam geometry.

16

With the preceding information, the fan angle, R/r, the diameter of the source-detector ring, the detector width, the multiplexing factor, the total number of detectors, and the number of pixels can be calculated as a function of N_a for a given flow diameter, total number of fan sources (fibers), and number of detectors per source. The results for several values of r, N_a, and n_d are shown in Table 2. As shown in the table (and as previously noted), w is nearly independent of the multiplexing factor. Assuming that the practical upper limit on the diameter and atmospheric pressure turbulent flow tube is 4 in., noting that the smallest turbulence scale size for this flow is ~ 1 mm (Ref. 40), requiring F_m to be an integer, and satisfying all the constraints mentioned in the preceding discussion, we can find a practical geometry. Such a geometry is shown in Fig. 4. In this figure, N_a = 6, θ = 30°, and F = 3.86. For a flow diameter of 4 in., 96 fibers, and 96 detectors per fan, the source-detecting ring diameter is 15.44 in. (39 cm), and w = 2.14 mm. These values yield a resolution of approximately 7000 pixels for a multiplexing factor of 16 and a total of 576 detectors.

B. NONPLANAR GEOMETRY

In the previous subsection, we considered the standard fan beam geometry, where the source and detector rings had equal radii. In this subsection, we briefly consider a nonplanar geometry, where these rings are still concentric with the flow but have different diameters (see Figs. 5 and 6). There are three disadvantages to a nonplanar design: (1) the reconstruction of the field from the projection data cannot be undertaken using some of the standard algorithms, (2) a right-angle cross section of the flow is no longer sampled, and (3) the instrument is optically more complex. These drawbacks may be outweighed by two important advantages. First, the detector width is no longer dictated solely by the flow diameter for a given resolution. Second, the radiation reflected from the transparent flow tube from the fan sources is not directed into the detectors. The fraction of light reflected from a fan is considered in Section III.B.

17

Table 2. Fan Geometries

FLOW DIAMETER(inches) = 4.00, DETECTORS/FAN =100., NUMBER OF FIBERS =100.

fans/circle	fan angle	D/d	D(cm)	detector(mm)	Multiplexing	# detectors	# pixels
2.0	90.00	1.41	14.37	2.26	50.00	200.	6368.
3.0	60.00	2.00	20.32	2.13	33.33	300.	7182.
4.0	45.00	2.61	26.55	2.09	25.00	400.	7458.
5.0	36.00	3.24	32.88	2.07	20.00	500.	7599.
6.0	30.00	3.88	39.28	2.06	16.67	600.	7676.
7.0	25.71	4.49	45.66	2.05	14.29	700.	7723.
8.0	22.50	5.13	52.08	2.05	12.50	800.	7754.
9.0	20.00	5.76	58.51	2.04	11.11	900.	7775.
10.0	18.00	6.39	64.95	2.04	10.00	1000.	7790.
11.0	16.36	7.03	71.39	2.04	9.09	1100.	7801.
12.0	15.00	7.66	77.84	2.04	8.33	1200.	7809.
13.0	13.85	8.30	84.29	2.04	7.69	1300.	7816.
14.0	12.86	8.93	90.74	2.04	7.14	1400.	7821.
15.0	12.00	9.57	97.20	2.04	6.67	1500.	7825.
16.0	11.25	10.20	103.66	2.04	6.25	1600.	7829.
17.0	10.59	10.84	110.11	2.03	5.88	1700.	7832.
18.0	10.00	11.47	116.57	2.03	5.56	1800.	7834.

FLOW DIAMETER(inches) = 8.00, DETECTORS/FAN =100., NUMBER OF FIBERS =100.

fans/circle	fan angle	D/d	D(cm)	detector(mm)	Multiplexing	# detectors	# pixels
2.0	90.00	1.41	21.55	3.39	50.00	200.	6368.
3.0	60.00	2.00	30.48	3.19	33.33	300.	7182.
4.0	45.00	2.61	39.82	3.13	25.00	400.	7458.
5.0	36.00	3.24	49.32	3.10	20.00	500.	7599.
6.0	30.00	3.88	58.88	3.08	16.67	600.	7676.
7.0	25.71	4.49	68.49	3.07	14.29	700.	7723.
8.0	22.50	5.13	78.12	3.07	12.50	800.	7754.
9.0	20.00	5.76	87.76	3.06	11.11	900.	7775.
10.0	18.00	6.39	97.42	3.06	10.00	1000.	7790.
11.0	16.36	7.03	107.09	3.06	9.09	1100.	7801.
12.0	15.00	7.66	116.78	3.06	8.33	1200.	7809.
13.0	13.85	8.30	126.43	3.06	7.69	1300.	7816.
14.0	12.86	8.93	136.11	3.05	7.14	1400.	7821.
15.0	12.00	9.57	145.80	3.05	6.67	1500.	7825.
16.0	11.25	10.20	155.48	3.05	6.25	1600.	7829.
17.0	10.59	10.84	165.17	3.05	5.88	1700.	7832.
18.0	10.00	11.47	174.86	3.05	5.56	1800.	7834.

18

Table 2. Fan Geometries (continued)

FLOW DIAMETER(inches) = 4.00,   DETECTORS/FAN = 75.,   NUMBER OF FIBERS =100.

fans/circle	fan angle	D/d	D(cm)	detector(mm)	Multiplexing	# detectors	# pixels
2.0	90.00	1.41	14.37	3.01	50.00	150.	3581.
3.0	60.00	2.00	20.32	2.84	33.33	225.	4029.
4.0	45.00	2.61	26.55	2.78	25.00	300.	4195.
5.0	36.00	3.24	32.88	2.75	20.00	375.	4274.
6.0	30.00	3.86	39.28	2.74	16.67	450.	4318.
7.0	25.71	4.49	45.68	2.73	14.29	525.	4344.
8.0	22.50	5.13	52.08	2.73	12.50	600.	4361.
9.0	20.00	5.78	58.51	2.72	11.11	675.	4373.
10.0	18.00	6.39	64.95	2.72	10.00	750.	4382.
11.0	16.36	7.03	71.39	2.72	9.09	825.	4388.
12.0	15.00	7.66	77.84	2.72	8.33	900.	4393.
13.0	13.85	8.30	84.29	2.72	7.69	975.	4396.
14.0	12.86	8.93	90.74	2.72	7.14	1050.	4399.
15.0	12.00	9.57	97.20	2.71	6.67	1125.	4402.
16.0	11.25	10.20	103.66	2.71	6.25	1200.	4404.
17.0	10.59	10.84	110.11	2.71	5.88	1275.	4405.
18.0	10.00	11.47	116.57	2.71	5.56	1350.	4407.

FLOW DIAMETER(inches) = 6.00,   DETECTORS/FAN = 75.,   NUMBER OF FIBERS =100.

fans/circle	fan angle	D/d	D(cm)	detector(mm)	Multiplexing	# detectors	# pixels
2.0	90.00	1.41	21.55	4.51	50.00	150.	3581.
3.0	60.00	2.00	30.48	4.26	33.33	225.	4029.
4.0	45.00	2.61	39.82	4.17	25.00	300.	4195.
5.0	36.00	3.24	49.32	4.13	20.00	375.	4274.
6.0	30.00	3.86	58.88	4.11	16.67	450.	4318.
7.0	25.71	4.49	68.49	4.10	14.29	525.	4344.
8.0	22.50	5.13	78.12	4.09	12.50	600.	4361.
9.0	20.00	5.76	87.76	4.08	11.11	675.	4373.
10.0	18.00	6.39	97.42	4.08	10.00	750.	4382.
11.0	16.36	7.03	107.09	4.08	9.09	825.	4388.
12.0	15.00	7.66	116.76	4.08	8.33	900.	4393.
13.0	13.85	8.30	126.43	4.07	7.69	975.	4396.
14.0	12.86	8.93	136.11	4.07	7.14	1050.	4399.
15.0	12.00	9.57	145.80	4.07	6.67	1125.	4402.
16.0	11.25	10.20	155.48	4.07	6.25	1200.	4404.
17.0	10.59	10.84	165.17	4.07	5.88	1275.	4405.
18.0	10.00	11.47	174.86	4.07	5.56	1350.	4407.

Table 2. Fan Geometries (continued)

FLOW DIAMETER(inches) = 4.00, NUMBER OF FIBERS =100.
DETECTORS/FAN = 50.,

fans/circle	fan angle	D/d	D(cm)	detector(mm)	Multiplexing	# detectors	# pixels
2.0	90.00	1.41	14.37	4.51	50.00	100.	1592.
3.0	60.00	2.00	20.32	4.28	33.33	150.	1790.
4.0	45.00	2.61	26.55	4.17	25.00	200.	1865.
5.0	36.00	3.24	32.88	4.13	20.00	250.	1900.
6.0	30.00	3.86	39.28	4.11	16.67	300.	1919.
7.0	25.71	4.49	45.68	4.10	14.29	350.	1931.
8.0	22.50	5.13	52.08	4.09	12.50	400.	1938.
9.0	20.00	5.78	58.51	4.08	11.11	450.	1944.
10.0	18.00	6.39	64.95	4.08	10.00	500.	1947.
11.0	16.36	7.03	71.39	4.08	9.09	550.	1950.
12.0	15.00	7.66	77.84	4.08	8.33	600.	1952.
13.0	13.85	8.30	84.29	4.07	7.69	650.	1954.
14.0	12.86	8.93	90.74	4.07	7.14	700.	1955.
15.0	12.00	9.57	97.20	4.07	6.67	750.	1956.
16.0	11.25	10.20	103.66	4.07	6.25	800.	1957.
17.0	10.59	10.84	110.11	4.07	5.88	850.	1958.
18.0	10.00	11.47	116.57	4.07	5.56	900.	1959.

FLOW DIAMETER(inches) = 6.00, NUMBER OF FIBERS =100.
DETECTORS/FAN = 50.,

| fans/circle	fan angle	D/d	D(cm)	detector(mm)	Multiplexing	# detectors	# pixels
2.0	90.00	1.41	21.55	6.77	50.00	100.	1592.
3.0	60.00	2.00	30.48	6.38	33.33	150.	1790.
4.0	45.00	2.61	39.82	6.26	25.00	200.	1865.
5.0	36.00	3.24	49.32	6.20	20.00	250.	1900.
6.0	30.00	3.86	58.88	6.17	16.67	300.	1919.
7.0	25.71	4.49	68.49	6.15	14.29	350.	1931.
8.0	22.50	5.13	78.12	6.14	12.50	400.	1938.
9.0	20.00	5.76	87.76	6.13	11.11	450.	1944.
10.0	18.00	6.39	97.42	6.12	10.00	500.	1947.
11.0	16.36	7.03	107.09	6.12	9.09	550.	1950.
12.0	15.00	7.66	116.76	6.11	8.33	600.	1952.
13.0	13.85	8.30	126.43	6.11	7.69	650.	1954.
14.0	12.86	8.93	136.11	6.11	7.14	700.	1955.
15.0	12.00	9.57	145.80	6.11	6.67	750.	1956.
16.0	11.25	10.20	155.48	6.11	6.25	800.	1957.
17.0	10.59	10.84	165.17	6.10	5.88	850.	1958.
18.0	10.00	11.47	174.86	6.10	5.56	900.	1959.

Table 2.   Fan Geometries (continued)

FLOW DIAMETER(inches) = 4.00,   DETECTORS/FAN = 75.,   NUMBER OF FIBERS = 75.

fans/circle	fan angle	D/d	D(cm)	detector(mm)	Multiplexing	# detectors	# pixels
2.0	90.00	1.41	14.37	3.01	37.50	150.	3581.
3.0	60.00	2.00	20.32	2.84	25.00	225.	4029.
4.0	45.00	2.61	26.55	2.78	18.75	300.	4195.
5.0	36.00	3.24	32.88	2.75	15.00	375.	4274.
6.0	30.00	3.88	39.28	2.74	12.50	450.	4318.
7.0	25.71	4.49	45.68	2.73	10.71	525.	4344.
8.0	22.50	5.13	52.08	2.73	9.38	600.	4361.
9.0	20.00	5.76	58.51	2.72	8.33	675.	4373.
10.0	18.00	6.39	64.95	2.72	7.50	750.	4382.
11.0	16.36	7.03	71.39	2.72	6.82	825.	4388.
12.0	15.00	7.66	77.84	2.72	6.25	900.	4393.
13.0	13.85	8.30	84.29	2.72	5.77	975.	4396.
14.0	12.86	8.93	90.74	2.72	5.36	1050.	4399.
15.0	12.00	9.57	97.20	2.71	5.00	1125.	4402.
16.0	11.25	10.20	103.66	2.71	4.69	1200.	4404.
17.0	10.59	10.84	110.11	2.71	4.41	1275.	4405.
18.0	10.00	11.47	116.57	2.71	4.17	1350.	4407.

FLOW DIAMETER(inches) = 6.00,   DETECTORS/FAN = 75.,   NUMBER OF FIBERS = 75.

fans/circle	fan angle	D/d	D(cm)	detector(mm)	Multiplexing	# detectors	# pixels
2.0	90.00	1.41	21.55	4.51	37.50	150.	3581.
3.0	60.00	2.00	30.48	4.26	25.00	225.	4029.
4.0	45.00	2.61	39.82	4.17	18.75	300.	4195.
5.0	36.00	3.24	49.32	4.13	15.00	375.	4274.
6.0	30.00	3.88	58.88	4.11	12.50	450.	4318.
7.0	25.71	4.49	68.49	4.10	10.71	525.	4344.
8.0	22.50	5.13	78.12	4.09	9.38	600.	4361.
9.0	20.00	5.76	87.76	4.08	8.33	675.	4373.
10.0	18.00	6.39	97.42	4.08	7.50	750.	4382.
11.0	16.36	7.03	107.09	4.08	6.82	825.	4388.
12.0	15.00	7.66	116.76	4.08	6.25	900.	4393.
13.0	13.85	8.30	126.43	4.07	5.77	975.	4396.
14.0	12.86	8.93	136.11	4.07	5.36	1050.	4399.
15.0	12.00	9.57	145.80	4.07	5.00	1125.	4402.
16.0	11.25	10.20	155.48	4.07	4.69	1200.	4404.
17.0	10.59	10.84	165.17	4.07	4.41	1275.	4405.
18.0	10.00	11.47	174.86	4.07	4.17	1350.	4407.
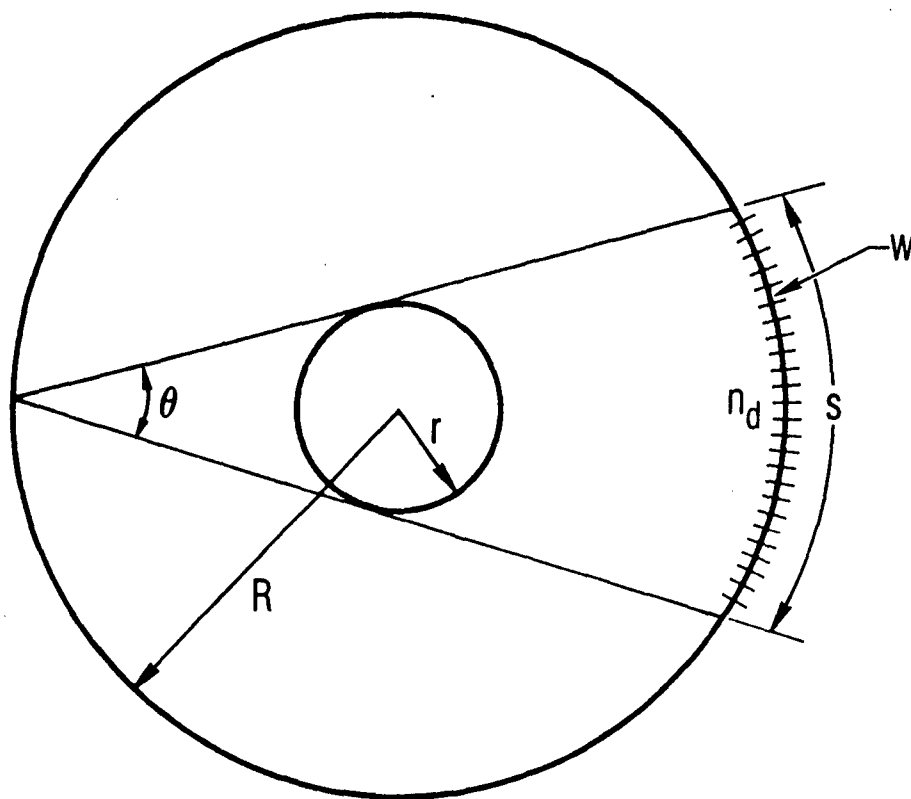
$$N_a = 6$$
$$\theta = 30°$$
$$F = 3.86$$

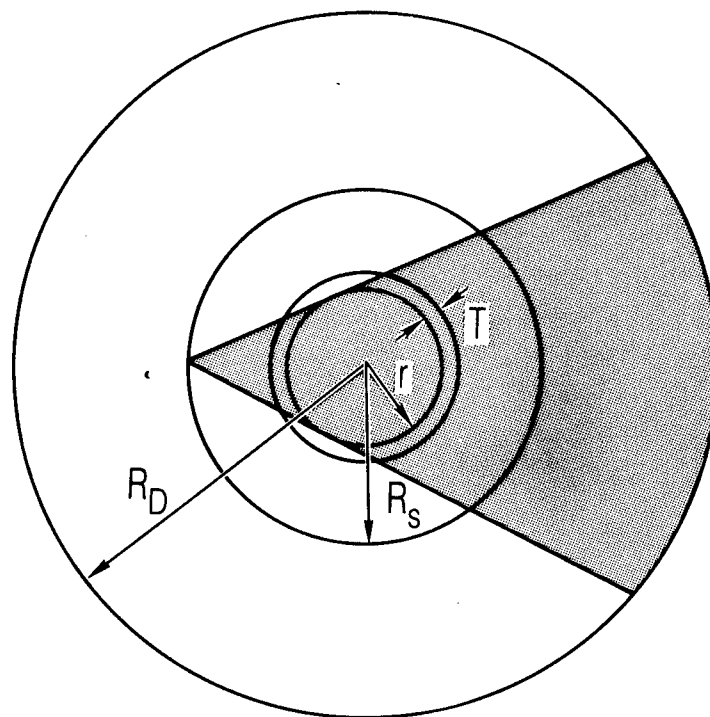Fig. 4. A Practical Geometry for Interrogating a Cylindrical Cross Section

Fig. 5.   Projected View of a Nonplanar Fan Beam Geometry. The source ring
radius R_s is smaller than the detector ring radius R_D.
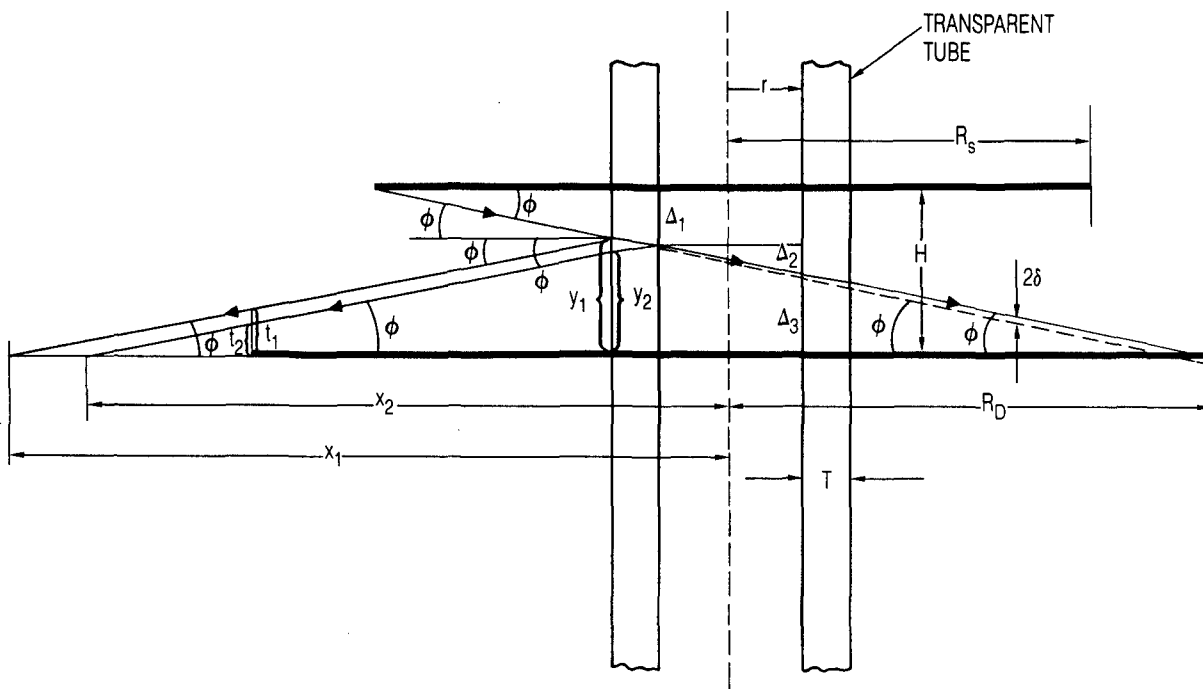
Fig. 6.   A Longitudinal View Along a Transparent Flow Tube Depicting the
          Displaced Structure of the Source Ring and Detector Ring of a
          Nonplanar Fan Beam Instrument. The ray emanating from the upper
          ring at angle ϕ is partially reflected from both surfaces of the
          tube before emerging from the opposite side of the tube parallel
          to, but displaced a distance δ from, the undeviated path.

Consider the side view of the nonplanar instrument shown in Fig. 6. A source ring of radius R_S is vertically displaced at height H from a detector ring of radius R_D. It is straightforward to show that a ray of light entering the side of the tube at incidence angle ϕ is displaced upward a distance

$$\delta = T \sin\phi \left(1 - \frac{\cos\phi}{\sqrt{n^2 - \sin^2\phi}}\right) \qquad (10)$$

where T is the thickness of the tube and n is its index of refraction. For a given T, R_S, R_D, and r, ϕ can be found as a function of H by requiring the ray to strike the detector ring, i.e.

$$H = \Delta_1 - \delta + \Delta_2 - \delta + \Delta_3 \qquad (11)$$

where

$$\Delta_1 = (R_S - r)\tan\phi$$

$$\Delta_2 = 2r \tan\phi$$

$$\Delta_3 = (R_D - r)\tan\phi$$

or

$$(R_S + R_D - 2r)\tan\phi - 2T\sin\phi \left(1 - \frac{\cos\phi}{\sqrt{n^2 - \sin^2\phi}}\right) - H = 0 \qquad (12)$$

In general, one wishes to choose H as small as possible, consistent with the requirement that the reflected rays from the inner or outer surfaces of the tube do not strike the detector ring. This requires $x_1 \neq R_D$ and $x_2 \neq R_D$, where

$$x_1 = \frac{y_1}{\tan\phi} + r + T \qquad (13)$$

$$x_2 = \frac{y_2}{\tan\phi} + r + T \qquad (14)$$

$$y_1 = H - (R_s - r - T)\tan\phi \qquad (15)$$

$$y_2 = y_1 - 2T \tan\phi' \qquad (16)$$

$$\phi' = \sin^{-1}\left(\frac{\sin\phi}{n}\right) \qquad (17)$$

Moreover, we require that the ray miss the detector by more than half the fan thickness, t_f, plus half the detector height, h_D, or

$$t_1 = (x_1 - R_D)\tan\phi > (t_f + h_D)/2 \qquad (18)$$

$$t_2 = (x_2 - R_D)\tan\phi > (t_f + h_D)/2 \qquad (19)$$

The procedure is to choose H as small as possible, keeping it greater than $t_f + h_D$ so the beam does not strike the opposite side of the source rings; to solve Eq. (12) for ϕ for the chosen H; then to check that inequalities in Eqs. (18) and (19) are satisfied.

Figure 7a displays the solution of Eq. (12) for $r = 2.0$ in., $T = 0.125$ in., $R_D/R_s = 3$, and $n = 1.5$ for $R_s/r = 2,3,4,6,8$. Figure 7b plots t_1, t_2, and $(t_f + h_D)/2$ for these values, letting $t_f = 1$ cm and $h_s = 1$ cm. Figure 7b indicates that the reflected rays intersect the detector ring between 5 and 6°. Thus, choosing a geometry where ϕ is less than 4° ensures that reflected radiation will not enter the detectors. These plots are not functions of R_s/r.
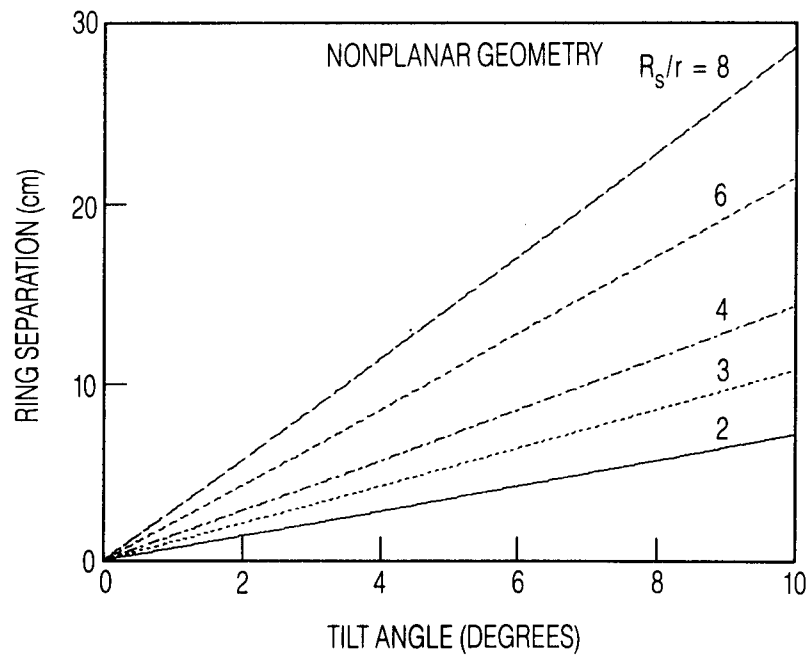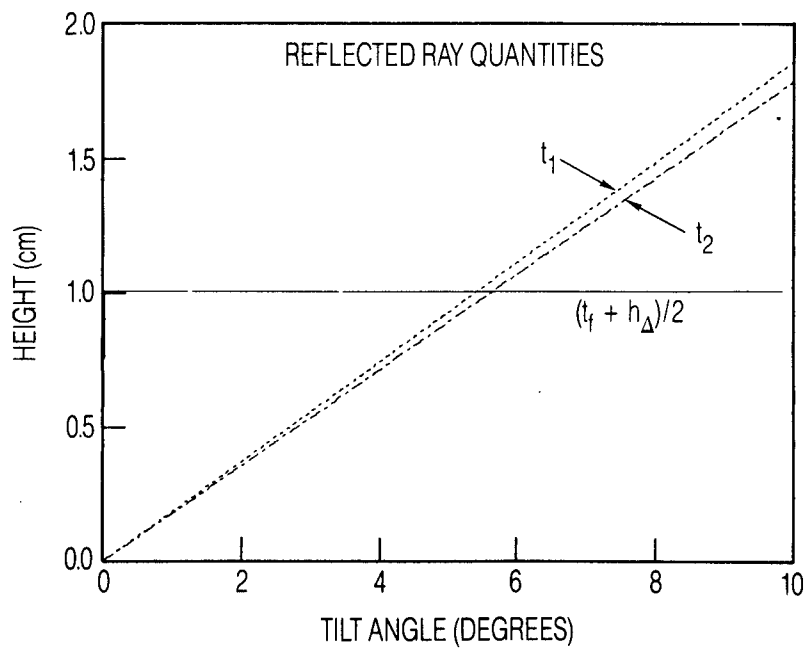
Fig. 7. (a) The Relationship Between the Tilt Angle ϕ shown in Fig. 6 and the Ring Separation in the Nonplanar Design; (b) Plot of the Reflection Quantities Discussed in Text. Only when the dashed curve intersects the solid curve does the reflected radiation from the first two surfaces of the tubes strike the detectors.

III. TUBE PERTURBATIONS

A. OVERVIEW

One of the more important applications of the proposed tomographic instrument is the interrogation of a flow confined in a cylindrical tube. The observation port should provide 360° access to the cross section of the flow at the position of interest. Ideally, the view port will be a short, transparent tube with the optical quality of an ophthalmic lens. This view port will be a glass, quartz, or sapphire thin-walled cylinder with an inner diameter equal to the diameter of the flow ($\sim$ 5-15 cm), a length of 1 to 2 cm, and a wall thickness of 2 to 6 mm. The view port will be positioned within the break of the insulated flow tube. The length of the port will be kept as small as possible to minimize thermal losses from the gas.

Figure 8 depicts a fan of radiation striking such a view port. A portion of each ray within the fan is reflected from the outer surface of the tube. In a planar instrument, this reflected radiation strikes one of the detectors on the source-detection ring. The portion of the ray that passes through the first surface continues to be divided and reflected around the tube, as shown in Fig. 8b for the ray launched at angle α. The transmitted intensities marked L_3, L_5, L_7, etc., escape the tube and, for the planar geometry, also strike the detectors. The transmitted intensity marked L_2 is the probe beam (the heavy line), which suffers a deviation as it passes through the four interfaces. The arc length displacement of this beam on the detector ring from its unperturbed position is marked Δs. The unperturbed trajectory (the dashed line) follows a different path through the gas than does the light ray. The mathematical algorithms used to reconstruct a cross section of the flow assume an undeviated path. The intensity transmitted through the first interface t_1 may be totally reflected at the second interface if the incidence angle at this interface is greater than the critical angle ($\simeq 41.8°$ for an index of refraction ratio of 1.5/1.0). The deviation of the ray is discussed in Section III.B. The problem of the reflected and transmitted intensities is considered in Section III.C.
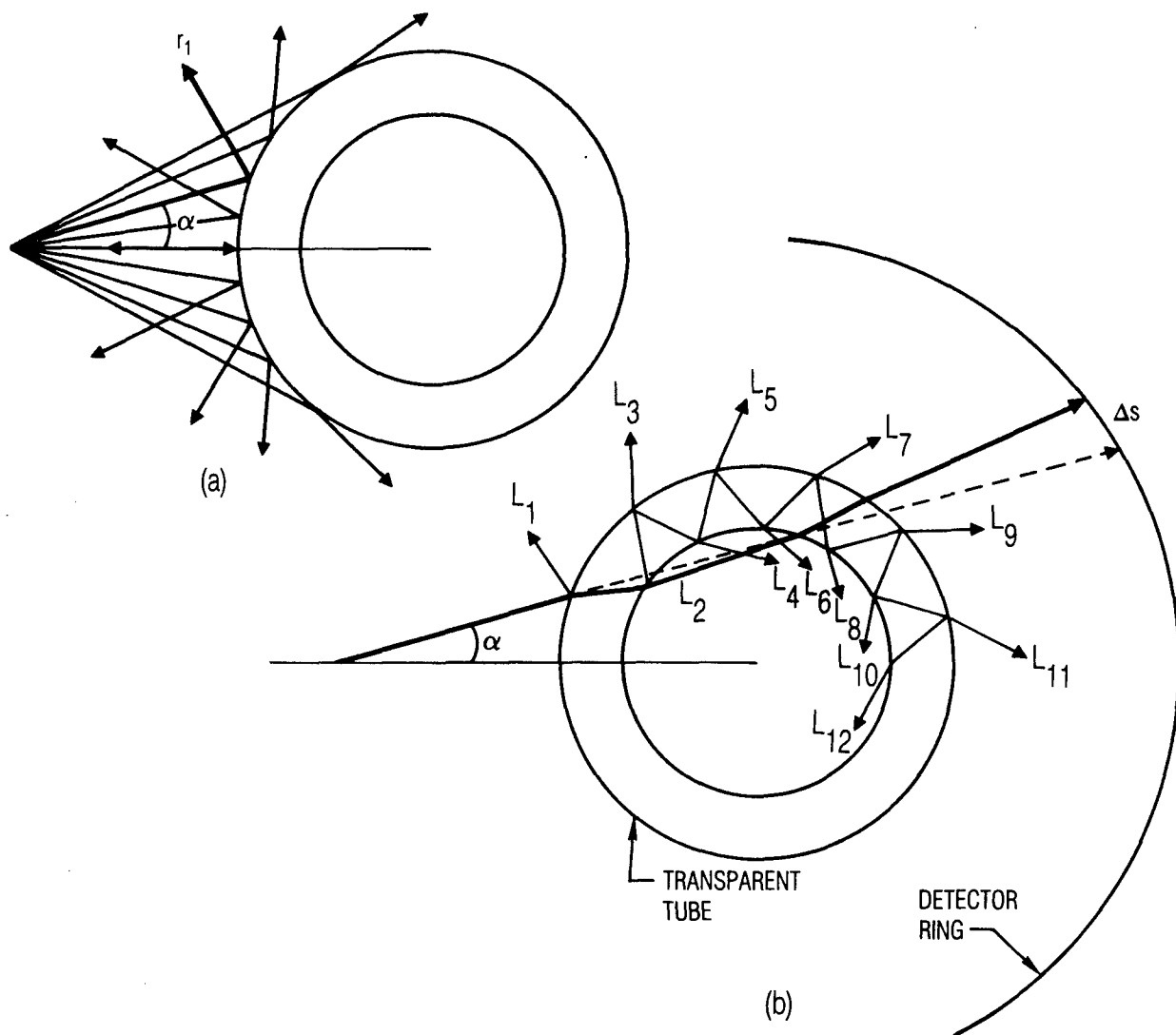
Fig. 8.   (a) Several Rays of a Fan Striking the Outside of a Transparent
Flow Tube; (b) The Fate of a Single Ray at Angle α in a Fan as It
Traverses the Tube and Strikes the Detector Ring.

30

B. RAY DEVIATION

The view port is equivalent to two cylindrical lenses separated by a distance equal to the sum of their outer (R_1) and inner (R_2) radii of curvature. Paraxial ray theory can be used to calculate the focal length of the left side of the tube

$$\frac{1}{f} = (n - 1)\left(\frac{1}{R_1} - \frac{1}{R_2}\right) \tag{20}$$

where R_1 (R_2) is the radius of curvature of the first (second) surface struck by the rays. The radius is positive if the center of curvature lies to the right of the surface and negative if it lies to the left of the surface. Accordingly, the radii are positive for the left side of the tube and negative for the right side of the tube. The net effect is that both sides of the tube act as negative (diverging) lenses. For example, if $|R_1|$ = 5.5 cm and $|R_2|$ = 5.0 cm, $f_1 = f_2 = -110$ cm. For two identical thin lenses separated by a distance d, the front and back focal lengths are identical and are given by (Ref. 41)

$$f_{fb} = \frac{f(d - f)}{d - 2f} \tag{21}$$

If $d = R_1 + R_2$, $f_{fb} = -57.5$ cm. Thin lens theory cannot be used to calculate correct deviations, even for thin-wall cylinders, because the geometries under consideration require large fan angles (nonparaxial rays). An exact ray trace calculation is required.

Consider the geometry shown in Figs. 9a and 10. A ray a distance d_i from the outer surface of the tube is launched at an angle α_i, which is a distance y_i above the horizontal. This ray strikes the tube surface at a point a height y_1 above the horizontal, making an angle β_1. We wish to calculate y_1 and β_1 as a function of R_1, α_i, y_i, and d_i. We note

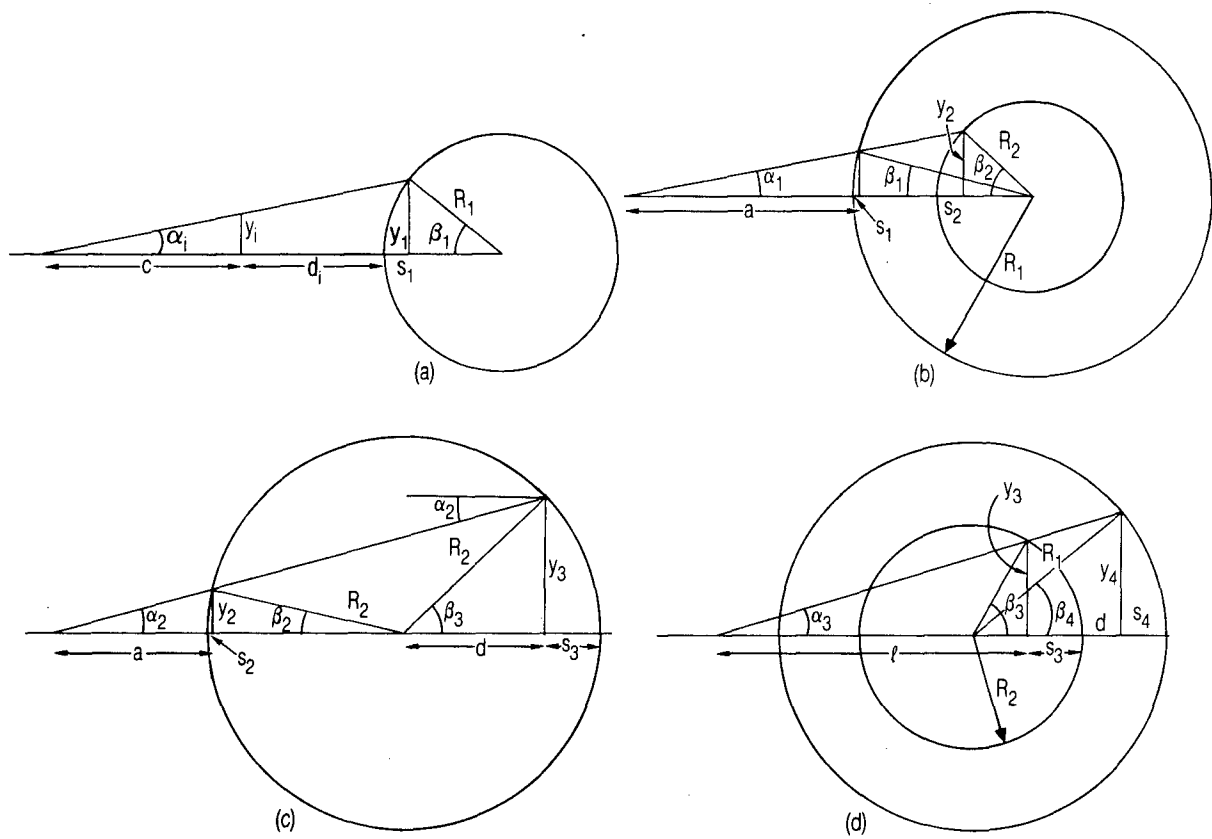$$y_1 = (c + d_i + s_1)\tan \alpha_i \tag{22}$$

31

Fig. 9. Definition of Parameters Used in Calculating the Exact Ray Path
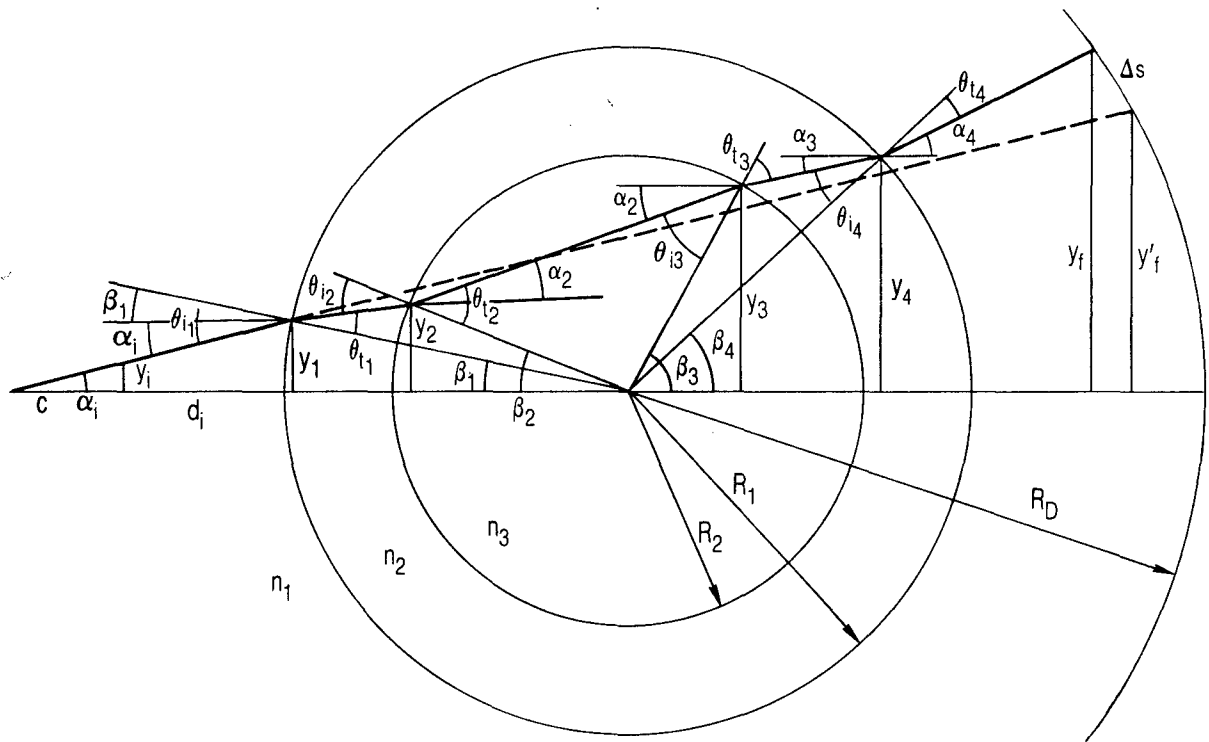Through the Tube

Fig. 10.   Composite View of Ray Traversing the Cross Section of Tube Defining Parameters Used in Calculating Ray Paths

33

$$s_1 = R_1 - R_1 \cos \beta_1 \tag{23}$$

$$c = y_i / \tan \alpha_i \tag{24}$$

$$y_1 = R_1 \sin \beta_1 \tag{25}$$

Substituting Eqs. (23)-(25) into Eq. (22) and solving, we find

$$\beta_1 = \cos^{-1} \left(\frac{kt + \sqrt{t^2 - k^2 + 1}}{t^2 + 1} \right) \tag{26}$$

where

$$k = [y_i + (d_i + R_1)t]/R_1 \tag{27}$$

$$t = \tan \alpha_i$$

and y_1 is given by Eq. (25).

Referring to Fig. 9b for the second surface, we wish to find β_2 and y_2, given y_1, α_1, β_1, R_1, and R_2. Here

$$y_2 = (a - s_1 + R_1 - R_2 + s_2)\tan \alpha_1 \tag{28}$$

$$s_2 = R_2(1 - \cos\beta_2) \tag{29}$$

$$a = y_1 / \tan\alpha_1 \tag{30}$$

$$y_2 = R_2 \sin \beta_2 \tag{31}$$

Substituting Eq. (23) and Eqs. (29)-(31) into Eq. (28), we find β_2 is given by Eq. (26), where

$$k = (y_1 + R_1 \; t \; \cos\beta_1)/R_2$$

$$\tag{32}$$

$$t = \tan\alpha_1$$

and y_2 is given by Eq. (31).

Surface 3 is shown in detail in Fig. 9c, where the unknowns β_3 and y_3 are obtained in terms of α_2, y_2, R_2, and β_2

$$y_3 = [(a - s_2) + 2R_2 - s_3]\tan\alpha_2 \tag{33}$$

$$a = y_2/\tan\alpha_2 \tag{34}$$

$$s_3 = R_2(1 - \cos\beta_3) \tag{35}$$

$$y_3 = R_2 \; \sin\beta_3 \tag{36}$$

Substituting Eq. (29) and Eqs. (34)-(36) into Eq. (33), we find β_3 is given by Eq. (26), where

$$k = y_2/R_2 - t \; \cos\beta_2$$

$$\tag{37}$$

$$t = -\tan\alpha_2$$

and y_3 is given by Eq. (36). The geometry for surface 4 is shown in Fig. 9d

$$y_4 = (\ell + s_3 + R_1 - R_2 - s_4)\tan\alpha_3 \tag{38}$$

$$\ell = y_3/\tan\alpha_3 \tag{39}$$

$$s_4 = R_1(1 - \cos\beta_4) \tag{40}$$

$$y_4 = R_1 \; \sin\beta_4 \tag{41}$$

Substituting Eq. (35) and Eqs. (39)-(41) into Eq. (38), we find β_4 is given by Eq. (26), where

$$k = (y_3 + R_2 t \cos\beta_3)/R_1$$

$$\text{(42)}$$

$$t = -\tan\alpha_3$$

and y_4 is given by Eq. (41).

The composite drawing is shown in Fig. 10. Each angle α must be related to the preceding α through Snell's law

$$n_i \sin\theta_i = n_t \sin\theta_t \qquad \text{(43)}$$

where θ_i (θ_t) is an incidence (transmitted) angle measured with respect to the surface normal and n is the index of the medium. Then for surface 1

$$\theta_{i1} = \alpha_i + \beta_1$$

$$\theta_{t1} = \sin^{-1}\left(\frac{n_1}{n_2} \sin\theta_{i1}\right) \qquad \text{(44)}$$

$$\alpha_1 = \theta_{t1} - \beta_1$$

for surface 2

$$\theta_{i2} = \alpha_1 + \beta_2$$

$$\theta_{t2} = \sin^{-1}\left(\frac{n_2}{n_3} \sin\theta_{i2}\right) \qquad \text{(45)}$$

$$\alpha_2 = \theta_{t2} - \beta_2$$

for surface 3

$$\theta_{i3} = \beta_3 - \alpha_2$$

$$\theta_{t3} = \sin^{-1}\left(\frac{n_3}{n_2} \sin \theta_{i3}\right) \tag{46}$$

$$\alpha_3 = \beta_3 - \theta_{t3}$$

and for surface 4

$$\theta_{i4} = \beta_4 - \alpha_3$$

$$\theta_{t4} = \sin^{-1}\left(\frac{n_2}{n_1} \sin \theta_{i4}\right) \tag{47}$$

$$\alpha_4 = \beta_4 - \theta_{t4}$$

Finally, we note that the ray strikes the detector ring at a height y_f

$$y_f = R_D \sin\beta_f \tag{48}$$

where β_f is given by Eq. (26) and

$$k = (y_4 + R_1 t \cos\beta_4)/R_D \tag{49}$$

$$t = -\tan\alpha_4$$

The ray would have struck the detector ring at height y_f' if the tube had not been present, where y_f' is given by

$$y_f' = R_D \sin\beta_f' \tag{50}$$

and β_f is given by Eq. (26), with

$$k = \left[y_i - (d_i + R_1)t\right]/R_D \tag{51}$$

$$t = -\tan \alpha_i$$

Finally, the arc length difference is

37

$$\Delta s = R_D (\beta_f' - \beta_f'') \tag{52}$$

Figure 11 shows the arc length deviation [Eq. (52)] as a function of angle within the fan for $N_a = 6$ for three tube inner diameters and three wall thicknesses. Table 3 lists the undeviated height [Eq. (50)], the ray-refracted height [Eq. (48)], and the arc length difference [Eq. (52)], where $N_a = 6$, $D = 4$ in., and $t = 1/8$ in. for 50 angles within a fan. These results clearly indicate that the deviations are large compared to the detector widths for all but the most central angles. Also, it is desirable to use as thin a wall as possible, and for a given tube thickness, as large an inner tube diameter as possible. This is because, for a given value of N_a, n_d, and n_f, the space available for the detector increases linearly with the flow diameter, whereas the deviations increase less than linearly with R_2. The expressions derived above can be used to preprocess the projection data before reconstruction of the cross section of flow or can be used to modify the reconstruction algorithm itself. Given the magnitude of those deviations, it may be necessary to limit the fan beam to the central three quarters of the flow and to use an onion peeling algorithm to help reconstruct the flow.

As noted in Section III.A, because the actual ray path and the undeviated ray path (dashed line in Fig. 10) are not the same inside the tube, an incorrect reconstructed field may result. The reconstruction algorithms assume that the undeviated path is taken. Correcting the algorithm only for the displacement Δs at the detector ring is acceptable only if the difference between the undeviated path and the actual path is less than or equal to the resolution (detector spacing).

Consider the difference between the coordinates of the end points of the two rays at the points where they intersect the inner wall of the tube. The coordinates of intersection of the undeviated ray with the inner circle of radius R_2 centered at the origin are
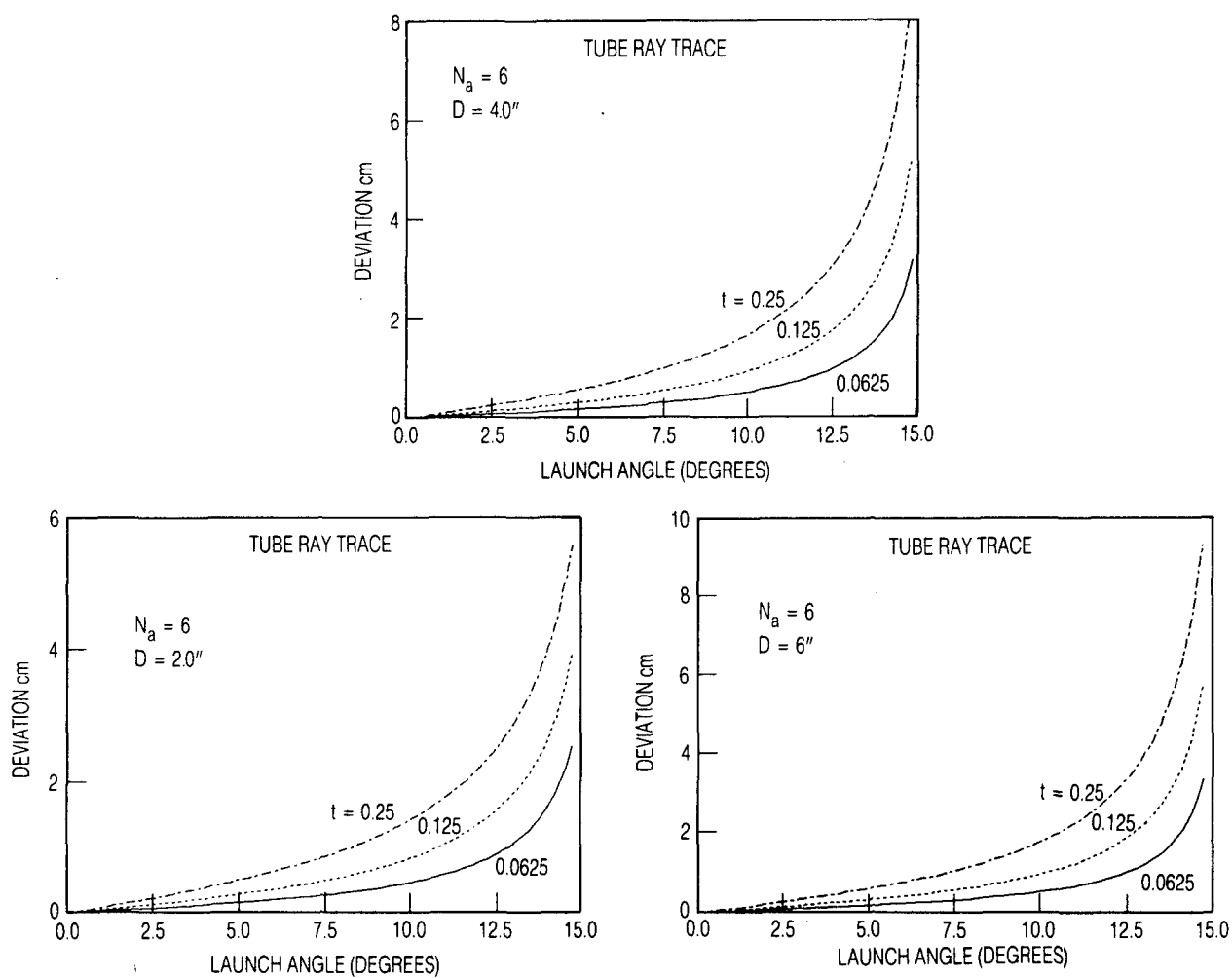
38

Fig. 11. Deviation at Detector Ring of Ray Passing Through a Tube for Three Different Inner Diameters and Three Wall Thicknesses

Table 3. Refraction Calculations for Tubes

D = 4.0 in., t = 1/8 in., N_a = 6

unch angle(rad)	undeviated ht(cm)	refracted ht(cm)	deviation(mm)
0.0052408	0.20547	0.22157	0.16102
0.0104816	0.41110	0.44354	0.32452
0.0157224	0.61654	0.66526	0.48746
0.0209632	0.82198	0.88712	0.65205
0.0262040	1.0273	1.1089	0.81763
0.0314448	1.2325	1.3308	0.98560
0.0366856	1.4375	1.5528	1.1560
0.0419264	1.6424	1.7748	1.3293
0.0471672	1.8471	1.9970	1.5058
0.0524080	2.0517	2.2193	1.6860
0.0576488	2.2560	2.4417	1.8707
0.0628896	2.4600	2.6643	2.0605
0.0681304	2.6638	2.8871	2.2553
0.0733712	2.8673	3.1101	2.4566
0.0786120	3.0705	3.3334	2.6646
0.0838528	3.2733	3.5569	2.8802
0.0890936	3.4758	3.7808	3.1040
0.0943344	3.6779	4.0051	3.3373
0.0995752	3.8796	4.2299	3.5808
0.1048160	4.0808	4.4552	3.8355
0.1100568	4.2817	4.6811	4.1031
0.1152976	4.4820	4.9077	4.3844
0.1205384	4.6819	5.1351	4.6811
0.1257792	4.8812	5.3634	4.9952
0.1310200	5.0800	5.5927	5.3284
0.1362608	5.2782	5.8233	5.6828
0.1415016	5.4759	6.0552	6.0611
0.1467424	5.6730	6.2888	6.4662
0.1519832	5.8694	6.5242	6.9015
0.1572240	6.0652	6.7617	7.3707
0.1624648	6.2603	7.0017	7.8788
0.1677056	6.4548	7.2447	8.4308
0.1729464	6.6485	7.4910	9.0334
0.1781872	6.8415	7.7413	9.6944
0.1834280	7.0338	7.9963	10.423
0.1886688	7.2252	8.2569	11.231
0.1939096	7.4159	8.5242	12.133
0.1991504	7.6058	8.7996	13.147
0.2043912	7.7948	9.0848	14.296
0.2096320	7.9830	9.3821	15.611
0.2148728	8.1703	9.6946	17.132
0.2201136	8.3567	10.026	18.914
0.2253544	8.5422	10.383	21.037
0.2305952	8.7267	10.773	23.615
0.2358360	8.9103	11.209	26.827
0.2410768	9.0929	11.712	30.971
0.2463176	9.2745	12.319	36.588
0.2515585	9.4551	13.102	44.829
0.2567993	9.6347	14.260	58.951

$$x'_{2,3} = \frac{-m_i^2 \ell \mp \sqrt{m_i^2(R_2^2 - \ell^2) + R_2^2}}{m_i^2 + 1}$$

(53)

$$y'_{2,3} = \sqrt{R_2^2 - x_{2,3}^2}$$

where x'_2, y'_2 (x'_3, y'_3) are the coordinates of the left (right) points of intersection in Fig. 10, $m_i = \tan\alpha_i$, and $\ell = c + d_i + R_1$. The y coordinates of the intersection of the actual ray at the inner tube radius are given by Eqs. (31) and (36). The x coordinates are then

$$x_{2,3} = (y_{2,3} - b_{1,2})/m_{1,2}$$

(54)

where $b_{1,2} = y_{1,2} - m_{1,2}x_{1,2}$, $m_{1,2} = \tan\alpha_{1,2}$, $x_1 = (y_1 - b_i)/m_i$, $b_i = y'_2 - m_i x'_2$, y_1 is given by Eq. (25), and $\alpha_{1,2}$ are given in Eqs. (44) and (45).

Figure 12 displays the results of the calculations for a 4.0 in. diameter flow and a tube thickness of 0.125 in. The quantities $(x_{2,3} - x'_{2,3})$, $(y_{2,3} - y'_{2,3})$, $[(x_{2,3} - x'_{2,3})^2 + (y_{2,3} - y'_{2,3})^2]^{1/2}$, and the normalized position of the crossing point of the two rays $(x_c - x_2)/(x_3 - x_2)$, $(y_c - y_2)/(y_3 - y_2)$ are shown in Figs. 12a, 12b, 12c, and 12d, respectively. The crossing coordinates are given by

$$x_c = (b_i - b_2)/(m_2 - m_i)$$

(55)

$$y_c = m_2 x_c + b_2$$

These results show that the deviations at the end points approach twice the detector spacing. This effect could degrade the resolution by a factor of ~ 2 near the inner wall of the tube if not corrected in the reconstruction algorithm.
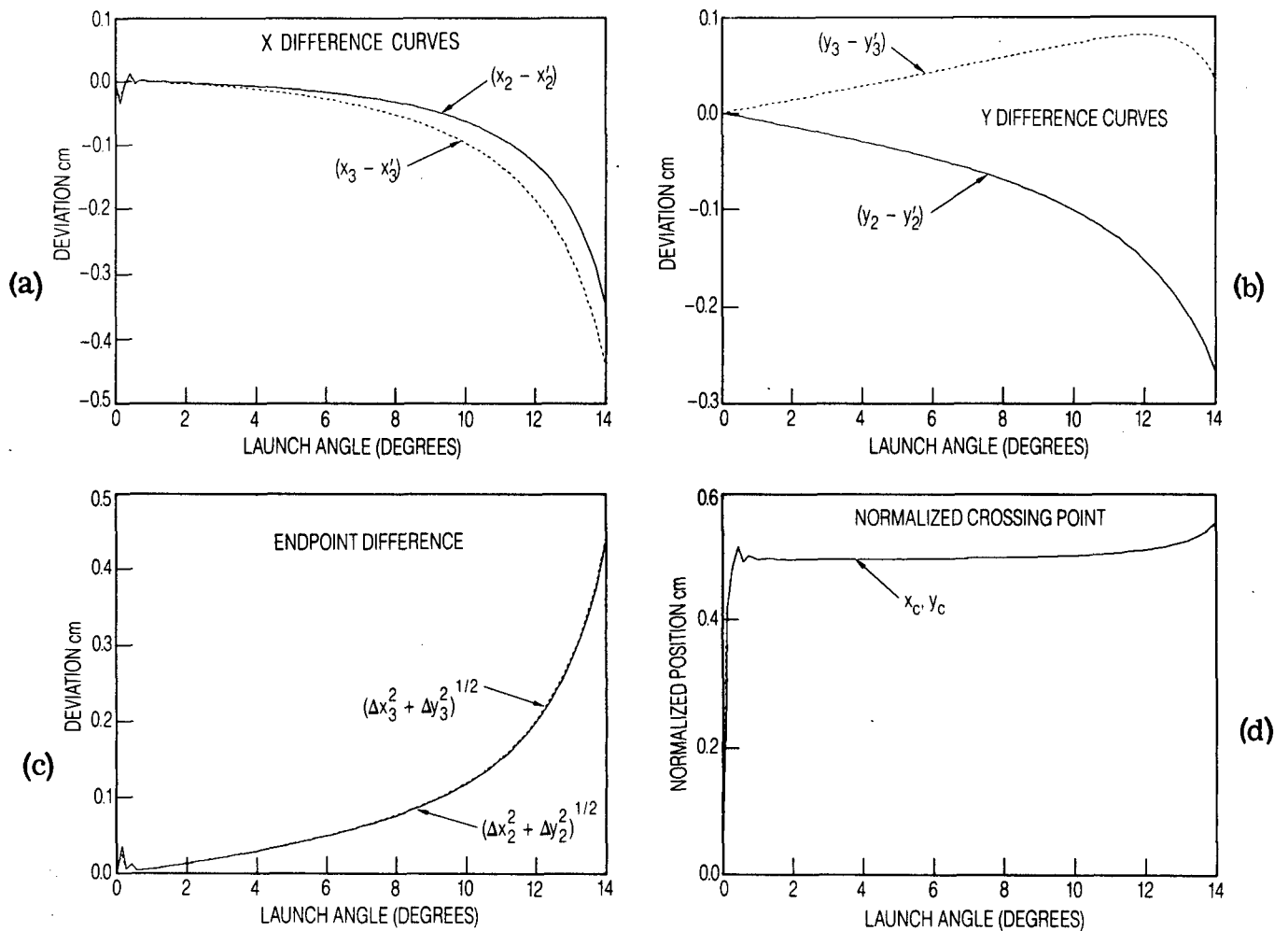
41

Fig. 12. Curves Depicting the Difference Between the Undeviated Ray and the Actual Ray Inside the Tube. (a) x coordinate differences at the ray intersection points with the tube inner wall; (b) y coordinate differences; (c) distance between the end points of the two rays at the inner wall intersection; (d) normalized crossing point. A value of 0.5 indicates crossing at the midpoint between the intersection of the actual ray with the inner wall.

C.   REFLECTION LOSSES

The intensities of the reflected and transmitted rays shown in Fig. 8 can be calculated using Fresnel's equations (Ref. 41)

$$R_\perp(\theta_i, \theta_t) = \left[\frac{\sin(\theta_i - \theta_t)}{\sin(\theta_i + \theta_t)}\right]^2 \tag{56}$$

$$R_{||}(\theta_i, \theta_t) = \left[\frac{\tan(\theta_i - \theta_t)}{\tan(\theta_i + \theta_t)}\right]^2 \tag{57}$$

$$T_\perp(\theta_i, \theta_t, n_i, n_t) = \left[\frac{2\sin\theta_t \cos\theta_i}{\sin(\theta_i + \theta_t)}\right]^2 \left(\frac{n_t \cos\theta_t}{n_i \cos\theta_i}\right) \tag{58}$$

$$T_{||}(\theta_i, \theta_t, n_i, n_t) = \left[\frac{2\sin\theta_t \cos\theta_i}{\sin(\theta_i + \theta_t)\cos(\theta_i - \theta_t)}\right]^2 \left(\frac{n_t \cos\theta_t}{n_i \cos\theta_i}\right) \tag{59}$$

where $R_\perp$ ($R_{||}$) and $T_\perp$ ($T_{||}$) are the reflected and transmitted intensities, respectively, for s-polarized (p-polarized) light. The incident ray in a medium with index n_i has an incident angle θ_i, is reflected from the surface with angle θ_r, and is transmitted into the medium with index n_t at angle θ_t. All angles are measured with respect to the surface normal. The angles are related through Snell's law [Eq. (43)] and the law of reflection, $\theta_i = \theta_r$.

Consider the geometry shown in Fig. 13. From $\triangle ABC$, $\delta_1 = \theta_{i2} - \theta_{r1}$; $\triangle BCD$, $\delta_2 = \theta_{i2} - \theta_{i3}$; $\triangle CDE$, $\delta_3 = \theta_{i4} - \theta_{i3}$; $\triangle CEF$, $\delta_4 = \theta_{i4} - \theta_{i5}$; etc. From $\triangle ABD$, $\theta_{r1} = \theta_{i3}$; $\triangle DEF$, $\theta_{i3} = \theta_{i5}$; etc. Thus, we conclude

$$\theta_{r1} = \theta_{i3} = \theta_{i5} = \theta_{i7} = \cdots \equiv \theta_{io} \tag{60}$$
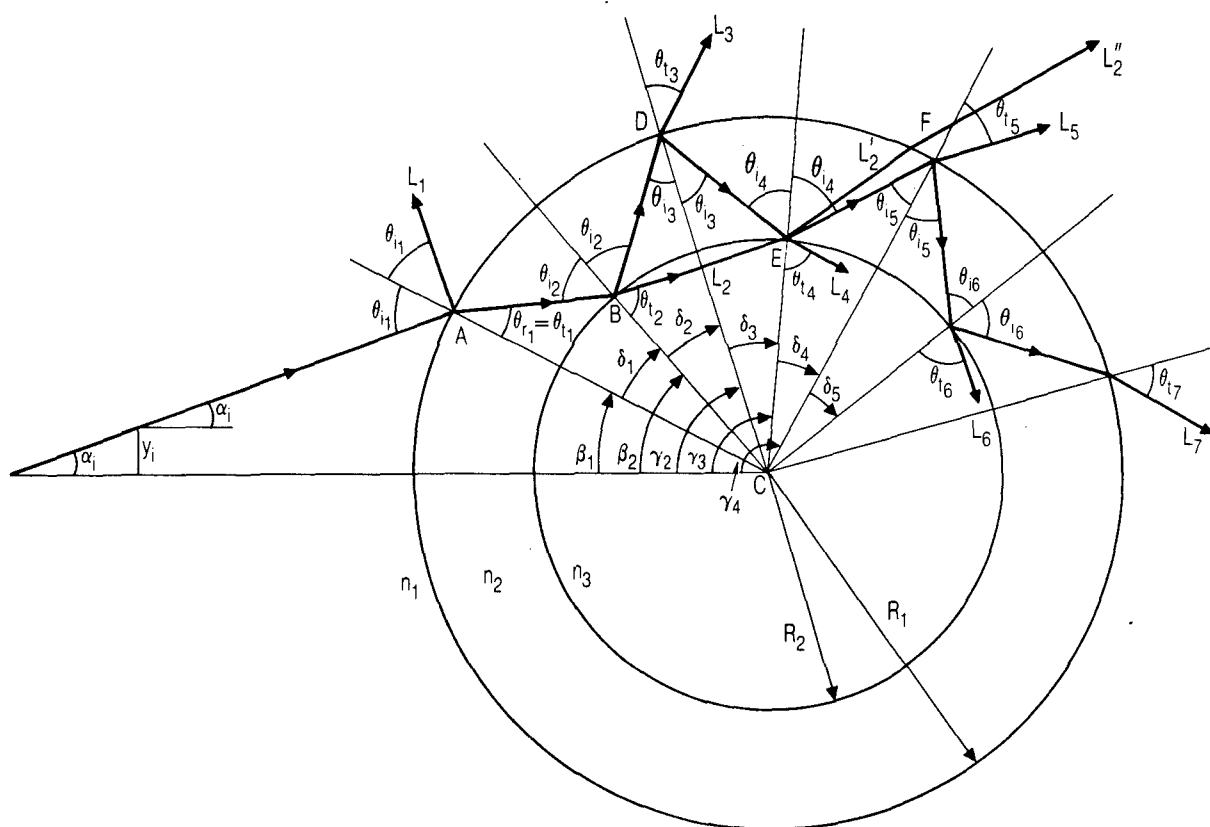
Fig. 13. Geometry and Definition of Parameters Used to Calculate the Intensities of the Reflected Radiation

$$\theta_{i2} = \theta_{i4} = \theta_{i6} = \theta_{i8} = \ldots \equiv \theta_{ie} \tag{61}$$

$$\delta_1 = \delta_2 = \delta_3 = \delta_4 = \ldots \equiv \delta = \beta_2 - \beta_1 \tag{62}$$

Because β_1, β_2, and θ_{i2} are known from the previous subsection [Eqs. (26), (27), (32), and (45)], θ_{ie} and δ are known. Thus, only θ_{io} must be found to have all angles of incidence. Angle θ_{io} is obtained from θ_{i3}. Applying the cosine law twice to $\triangle BCD$, we have

$$\overline{BD} = R_1^2 + R_2^2 - 2R_1R_2 \cos\delta$$

$$R_2^2 = (\overline{BD})^2 + R_1^2 - 2 (\overline{BD}) R_1 \cos\theta_{i3}$$

Solving for θ_{i3}, we find

$$\theta_{io} = \theta_{i3} = \cos^{-1} \left[\frac{R_1 - R_2 \cos\delta}{(R_1^2 + R_2^2 - 2R_1R_2 \cos\delta)^{1/2}} \right] \tag{63}$$

Finally, the angles of transmission (refraction) are obtained from Eq. (43)

$$\theta_{te} = \sin^{-1} \left[\frac{n_2}{n_3} \sin \theta_{ie} \right]$$

$$\theta_{to} = \sin^{-1} \left[\frac{n_2}{n_1} \sin \theta_{io} \right] \tag{64}$$

If the intensity of the incident ray is assigned a normalized value of 1, then the intensities of the beams labeled L_n, where $n = 1,2,3$, etc., are

$$L_1 \quad = R_1$$

$$L_2 \quad = T_1 T_e$$

$$L_3 \quad = T_1 R_e T_o \tag{65}$$

$$L_{2n} \quad = (R_e R_o)^{n-1} L_2$$

$$L_{2n+1} = (R_e R_o)^{n-1} L_3$$

In these relations, n refers to the surface encountered, and we used

$$R_2 = R_4 = R_6 = \dots \equiv R_e$$

$$R_3 = R_5 = R_7 = \dots \equiv R_o$$

$$\tag{66}$$

$$T_2 = T_4 = T_6 = \dots \equiv T_e$$

$$T_3 = T_5 = T_7 = \dots \equiv T_o$$

The signal beam is intensity L_2. All other values of L_n are losses from this signal beam. The total exterior and interior losses are

$$L^T E = \sum_{n=0}^{\infty} L_{2n+1} \tag{67}$$

$$L^T I = \sum_{n=2}^{\infty} L_{2n} \tag{68}$$

46

Finally, the intensity of a beam traversing the entire tube (the projection of L_2 through the second wall) is

$$L_2'' = L_2 T_3' T_4'$$ (69)

where T_3' and T_4' are Eqs. (58) and (59) evaluated for the incident and transmitted angles at the back two interfaces of the tube wall. Total internal reflection occurs at dense-to-rare interfaces when the angle of the transmitted beam is $\geq 90°$, that is, when

$$\sin \theta_{ie} \geq \frac{n_3}{n_2}$$ (70a)

or

$$\sin \theta_{io} \geq \frac{n_1}{n_2}$$ (70b)

Fan beam geometries that satisfy either Eqs. (70a) or (70b) must be avoided.

Equations (56)-(69) can be used to calculate all relevant intensities in the fan beam. Figures 14-18 exhibit the results of some of these calculations. Figures 14-15 display the intensities of the transmitted beam (L_2''), the interior transmitted beam (L_2), the first surface reflection loss (L_1), the first transmitted loss out of the tube (L_3), the total external loss [Eq. (67)], and the total internal loss [Eq. (68)], for s-, p-, and unpolarized beams as a function of ray angle within the fan beam for N = 6; an inner diameter of 4 in.; and tube wall thicknesses of 1/8 and 1/4 in. Figures 16 and 17 exhibit the same calculations for a tube with an inner diameter of 6 in. and wall thicknesses of 1/8 and 1/4 in. Figure 18 displays results for a 6 in. tube with N = 3.

From these curves, we can draw a number of conclusions. The first surface reflection loss is greater for the 6 in. tube than for the 4 in. tube (13% vs 10%) and is greater for the 1/8 in. wall than for the 1/4 in. tube (10% vs 13% at the maximum ray angle). The transmitted beam intensity
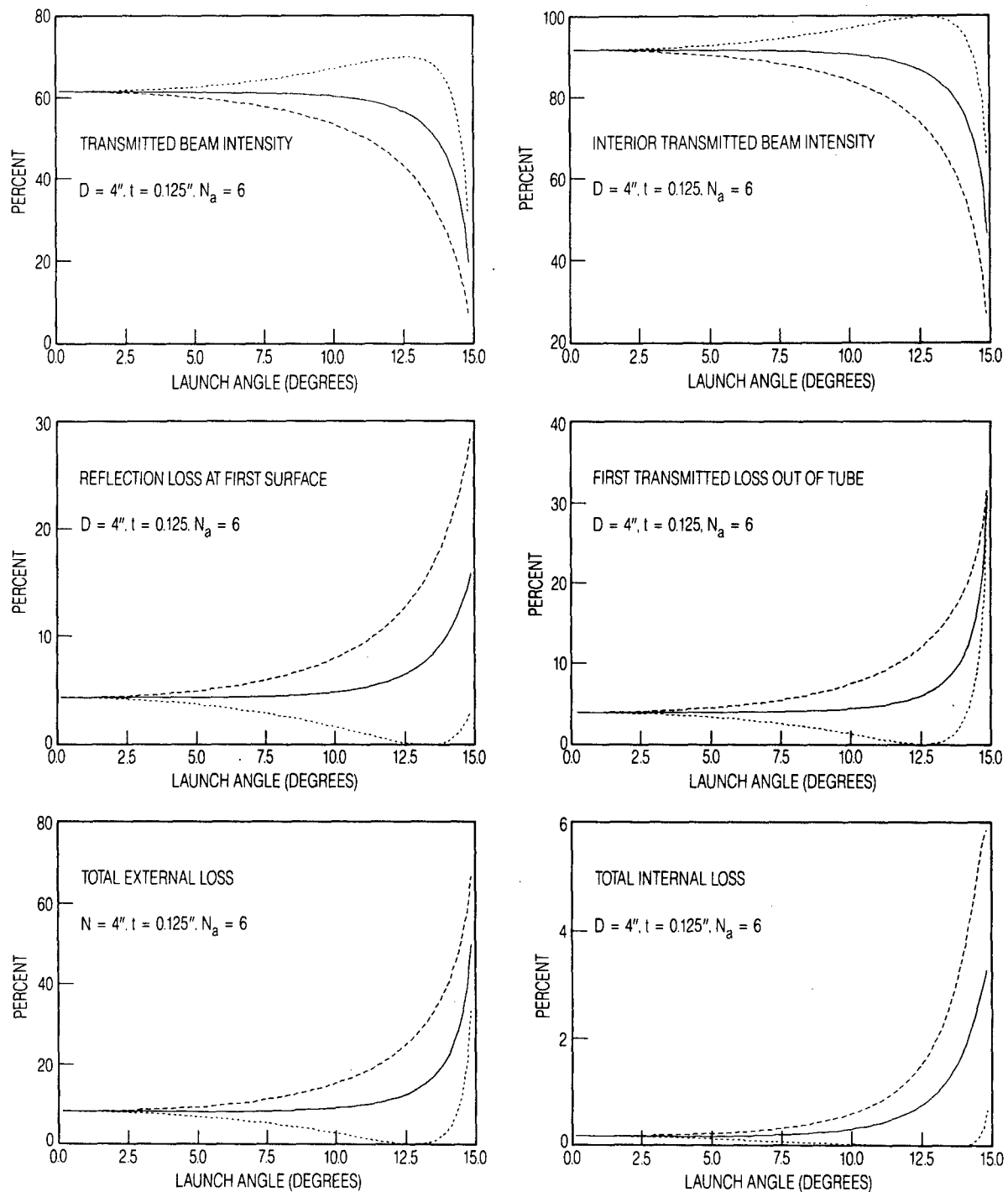
Fig. 14. Reflected and Transmitted Intensities for All Ray Angles Within a
Fan for Flow Diameter of 4 in., Tube Wall Thickness of 0.125 in.,
and N_a = 6

Fig. 15. Reflected and Transmitted Intensities for all Ray Angles Within a Fan for Flow Diameter of 4 in., Tube Wall Thickness of 0.25 in., and N_a = 6

49

Fig. 16. Reflected and Transmitted Intensities for All Ray Angles Within a Fan for Flow Diameter of 6 in., Tube Wall Thickness of 0.125 in., and $N_a = 6$
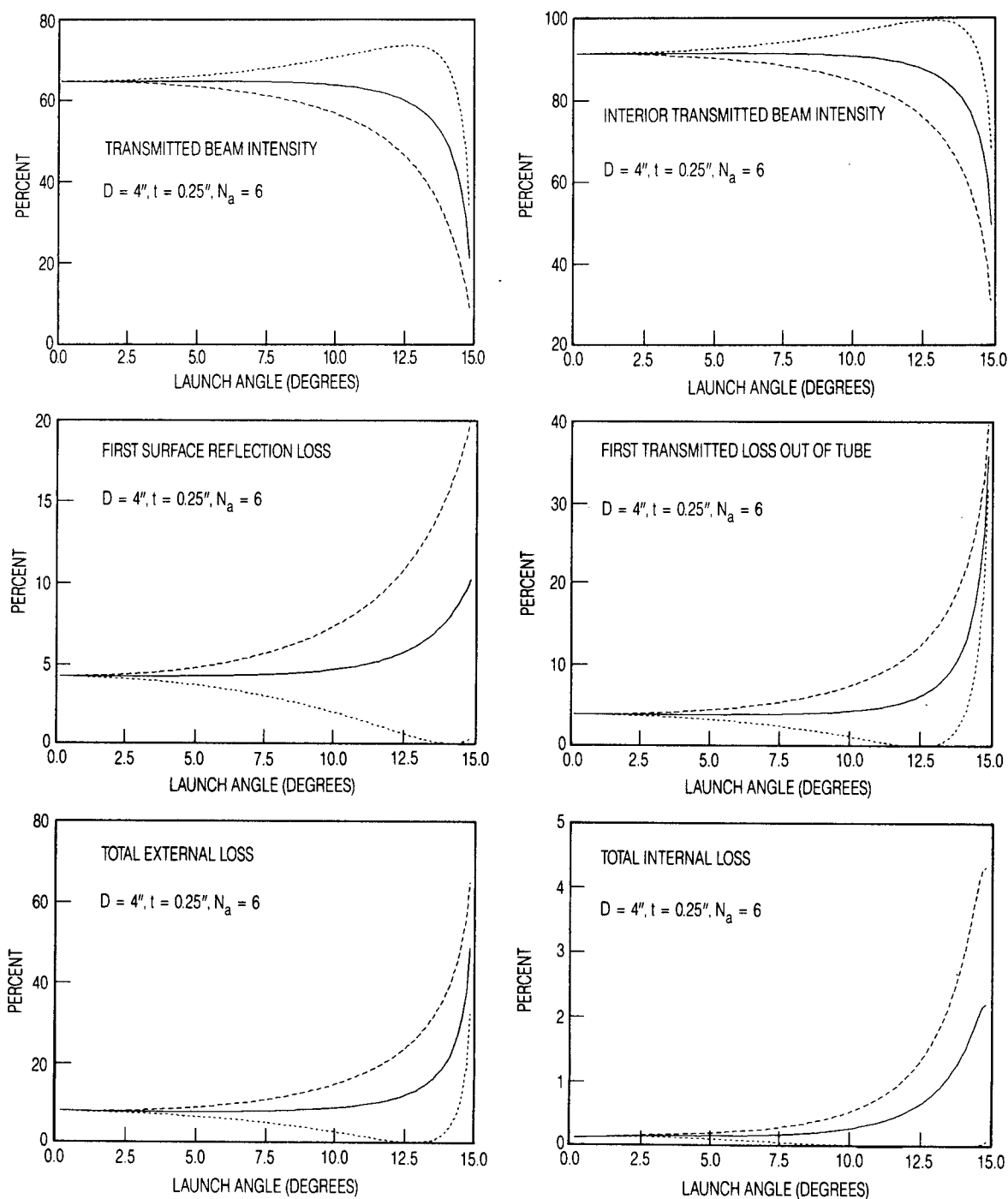
50
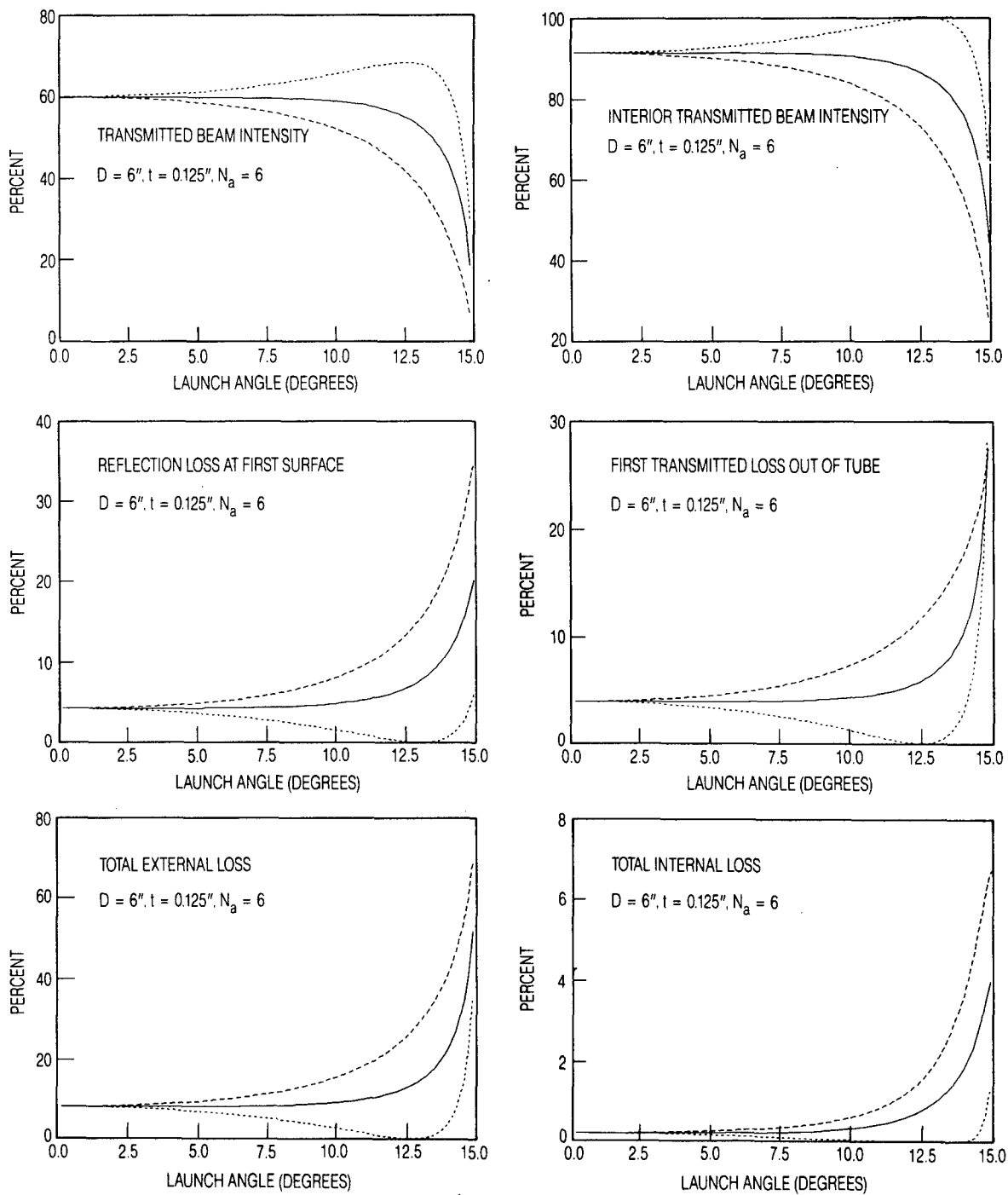
Fig. 17. Reflected and Transmitted Intensities for All Ray Angles Within a Fan for Flow Diameter of 6 in., Tube Wall Thickness of 0.25 in., and $N_a = 6$

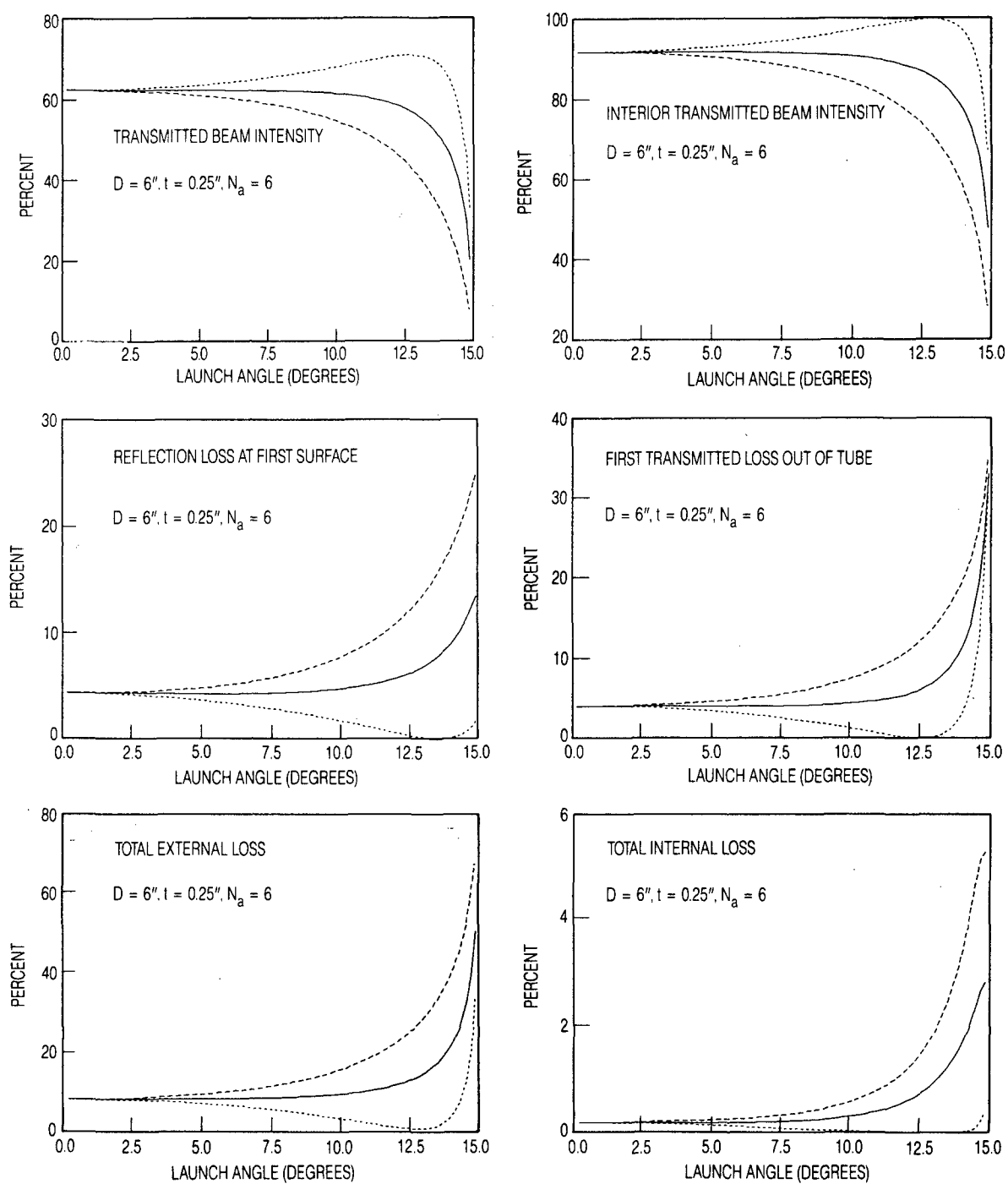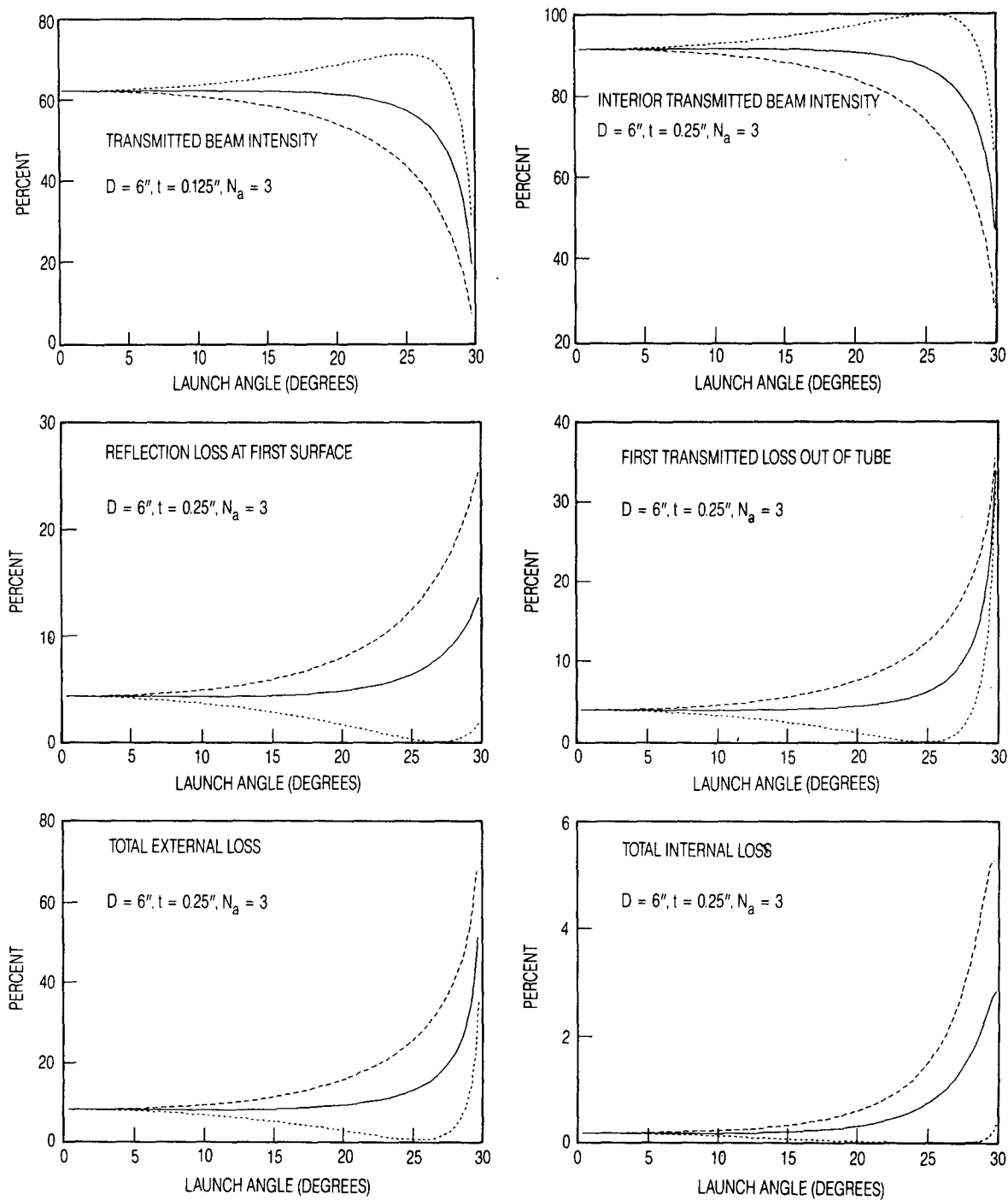51

Fig. 18. Reflected and Transmitted Intensities for All Ray Angles Within a Fan for Flow Diameter of 6 in., Tube Wall Thickness of 0.25 in., and N_a = 3

is slightly better for the 4 in. tube than for the 6 in. tube (by 1 to 2% at high ray angles) and is slightly better for the 1/4 in. wall than for the 1/8 in. wall. The first transmitted loss out of the tube (L_3) is somewhat greater for the 4 in. tube and is greater for the 1/4 in. wall (35% vs 28%). The total external loss is the same for both tube diameters and very slightly greater for the 1/8 in. tube than for the 1/4 in. tube. The total internal loss is greater for the 6 in. diameter tube than for the 4 in. diameter tube (3% vs ~ 2%) and is greater for the 1/8 in. wall than for the 1/4 in. wall (4% vs 3%). No significant difference is seen between the $N = 3$ and $N = 6$ calculations. In general, the 4 in. diameter tube is slightly better than the 6 in. diameter tube, and the 1/4 in. wall is slightly better than the 1/8 in. wall.

These curves indicate that it would be significantly better to use p-polarized light. Unfortunately, polarization-preserving fibers currently exist only for single-mode optic fibers. Because of the high intensities experienced during a short (nanosecond) laser pulse, only multimode, macrofibers are relevant to this work.

In summary, the calculations from this subsection and the previous subsection favor a thin-walled, 4 in. diameter flow tube view port.

IV. FAN BEAM DISTORTION CAUSED BY THE GAS

Variation of the index of refraction of the gas causes distortion in the fan beam. The index is a function of the gas density which, in turn, depends on the temperature and pressure. For flow tube applications, pressure gradients are expected to be small, and temperature variations cause the principal distortions of the rays. In this section, we consider the deviation of a ray in the fan beam due to a cylindrically symmetric temperature variation.

The path of a ray traversing a medium with a continuously varying index of refraction is given by (Ref. 42)

$$\frac{d}{ds}\left(n \frac{d\vec{r}}{ds}\right) = \vec{\nabla}n \tag{71}$$

where $\vec{r}$ is the position vector along the ray path and s is the path length. If we refer to the geometry shown in Fig. 19a, Eq. (71) can be written

$$\theta(y_i) = \frac{1}{n_o} \int_{-\infty}^{\infty} \left.\frac{\partial\delta}{\partial y}\right|_{y_i} dx \tag{72}$$

where $n = 1 + \delta$, n_o is the index of the unperturbed medium, $\frac{d\vec{r}}{ds} = \theta(y_i)$, and it is assumed that the variation of the index is small compared to 1 (paraxial approximation). This approximation is always true for gases at or below atmospheric pressure and allows $ds = dx$ and $\frac{\partial\delta}{\partial s} = \frac{\partial\delta}{\partial y}$. If we transform Eq. (72) to polar coordinates, assuming δ is a function of r only (cylindrical symmetry), noting that the integrand is an even function of x and that $\frac{\partial\delta}{\partial r} = 0$ for $r > R$, we have

$$\theta(y_i) = \frac{2y_i}{n_o} \int_{y_i}^{R} \frac{\partial\delta(r)}{\partial r} \left(r^2 - y_i^2\right)^{-1/2} dr \tag{73}$$
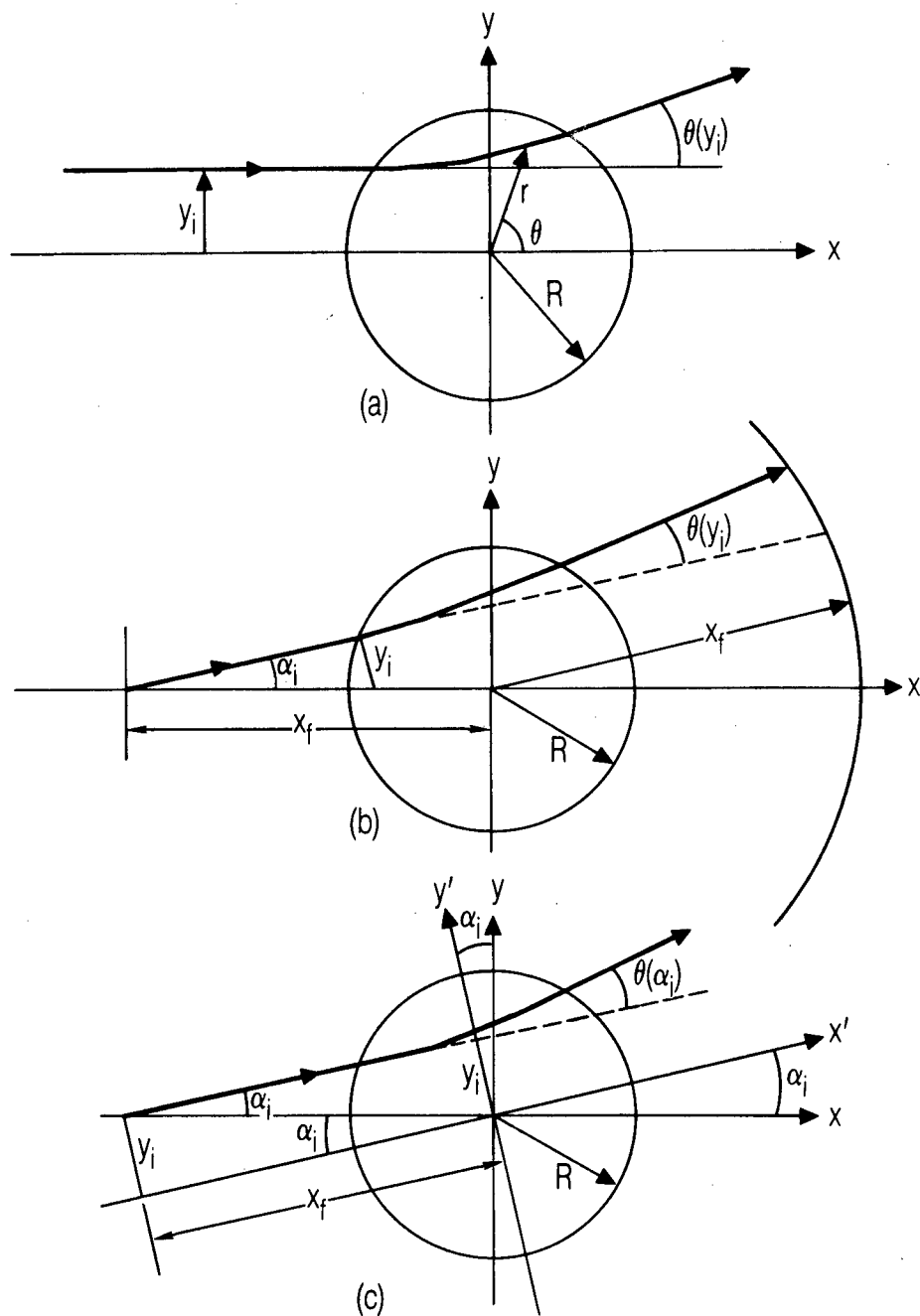
55

Fig. 19. Definition of Quantities Used to Calculate the Ray Deviation Caused by a Cylindrically Symmetric, Continuously Varying Index of Refraction

For a fan beam geometry, we wish to find $\theta(\alpha_i)$, where α_i is the angle of ray (i) in the fan (Fig. 19b). The relationship between y_i and α_i is especially simple for cylindrical symmetry, because each value of α_i corresponds to a new y_i. Figure 19c indicates that a ray launched at angle α_i in Fig. 19b has exactly the same geometry as Fig. 19a with a new coordinate system (x',y') if the flow has cylindrical symmetry. Accordingly

$$y_i = x_f \tan\alpha_i \tag{74}$$

The index of refraction of a gas is a function of the density, i.e.

$$(n - 1) = \delta \propto \rho$$

For constant pressure and an ideal gas

$$\delta = \frac{C}{T}$$

where C is a constant and T is the absolute temperature in Kelvin. Noting $\delta_{NPT} = 0.000293$, we have $C = 8.79 \times 10^{-2}$ K. If the temperature at the center of the flow is T_m, the edge temperature is T_o and we allow the temperature to vary as a power of r between these values, i.e.

$$T(r) = T_m - kr^n \quad n = 1,2,3,\ldots$$

where $\tag{75}$

$$k = (T_m - T_o)/R^n$$

Then

$$\delta(r) = C\left(T_m - kr^n\right)^{-1} \tag{76}$$

and the gradient of the index becomes

$$\frac{d\delta(r)}{dr} = nkCr^{(n-1)}/(T_m - kr^n)^2 \tag{77}$$

Using Eqs. (77) and (74) in Eq. (73), and numerically integrating Eq. (73), we can calculate the deviation as a function of α_i, geometry, T_o, T_m, and temperature gradient. The results of these calculations for several geometries and for five powers of r (linear through r^5) are given in Figs. 20 and 21. These results indicate that, in all cases, the deviations at the detector ring caused by the temperature gradients are small compared to the detector width (w = 2 mm for D = 4 in. and w = 3 mm for D = 6 in.). The curves also indicate that the deviations increase with increasing N_a and D. This increase is expected because the detector-ring diameter increases with both of these parameters. The deviations are very sensitive to the difference between the center and edge temperatures. In Fig. 21, changing the edge temperature from 300 to 500 K reduces the maximum deviation by nearly a factor of 3. In all curves, in the angular central two-thirds of the tube, the deviation is nearly independent of the functional form of the temperature gradient. Thus, if the peak and edge average temperatures can be estimated, average corrections can be applied to this region, either a priori or iteratively.

This calculation can also be used to estimate the ray deviation caused by a turbulence cell. Figure 22 exhibits the deviation at the detector ring due to a 2 mm diameter bubble with a center-to-edge density variation of a factor of 2. At high angles and for radial variations of $\sim r^2$-r^3, the deviation is approximately 0.05 mm. This value is not a strong function of the size of the structure. A nonrandom cumulative effect of several such structures could be appreciable and might restrict the degree of turbulence tolerable for high-resolution imaging.

Last, we note that the index of refraction of a medium changes rapidly near an absorption, as shown in Fig. 23. The refractive index n varies from less than 1 to greater than 1 as radiation is scanned across an absorption curve. This is not a problem for frequency-stable radiation

58
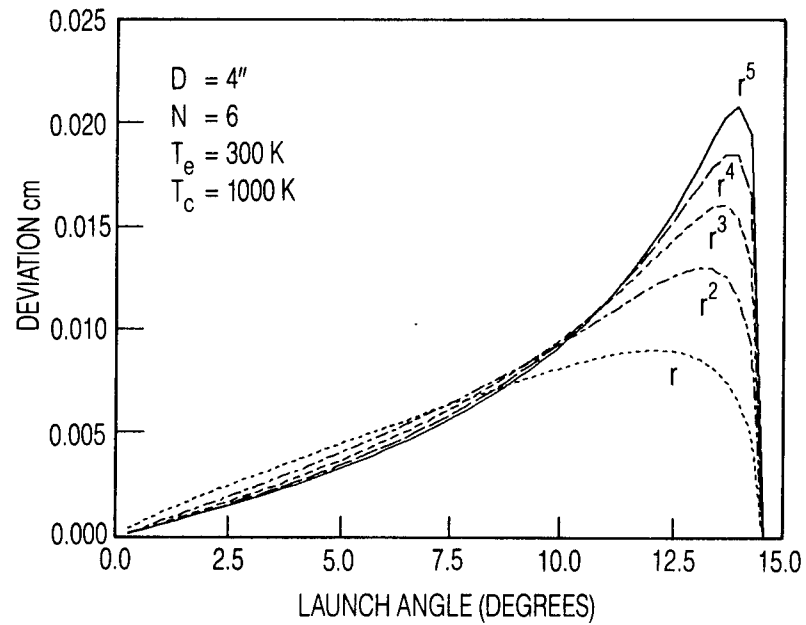
Fig. 20. Deviation at the Detector Ring of a Ray Passing Through a 4 in. Diameter Flow with a Cylindrically Symmetric Variation in Temperature for Five Different Temperature Gradients

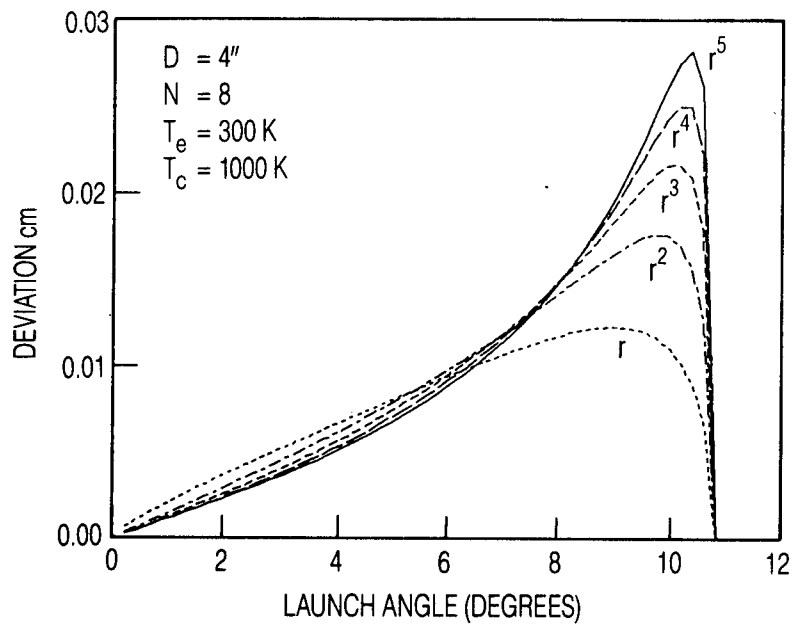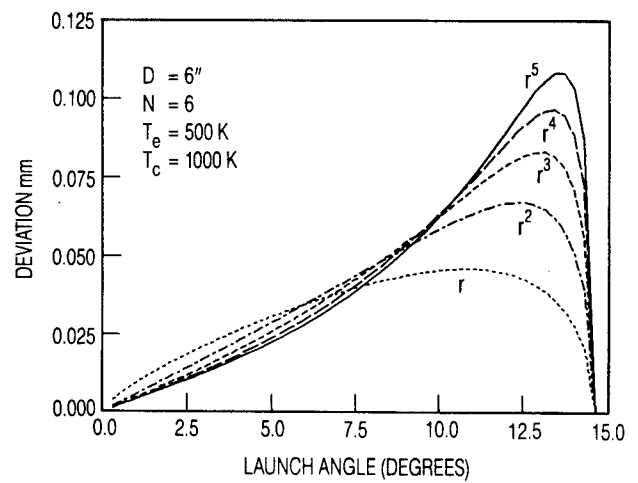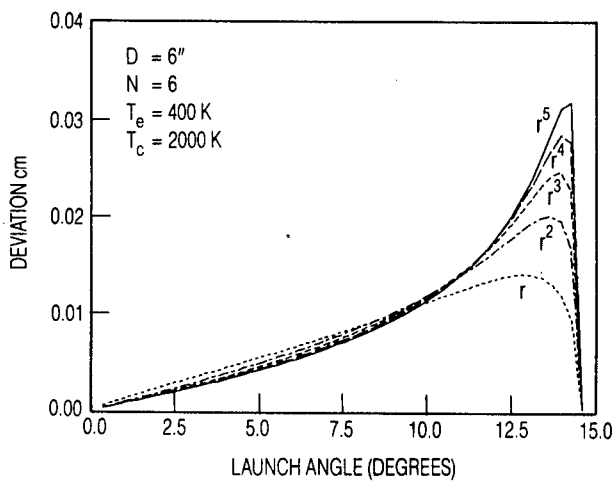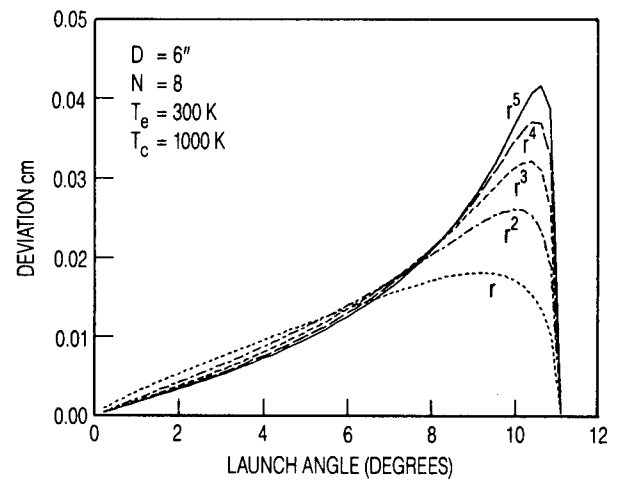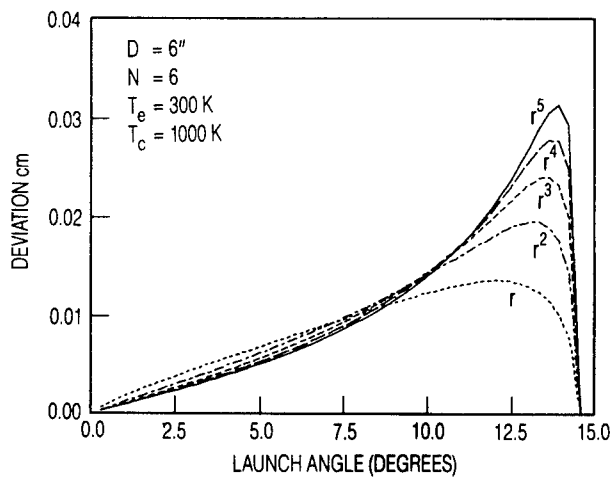Fig. 21. Deviation at the Detector Ring of a Ray Passing Through a 6 in.
Diameter Flow with a Cylindrically Symmetric Variation in Tem-
perature for Five Different Temperature Gradients

60
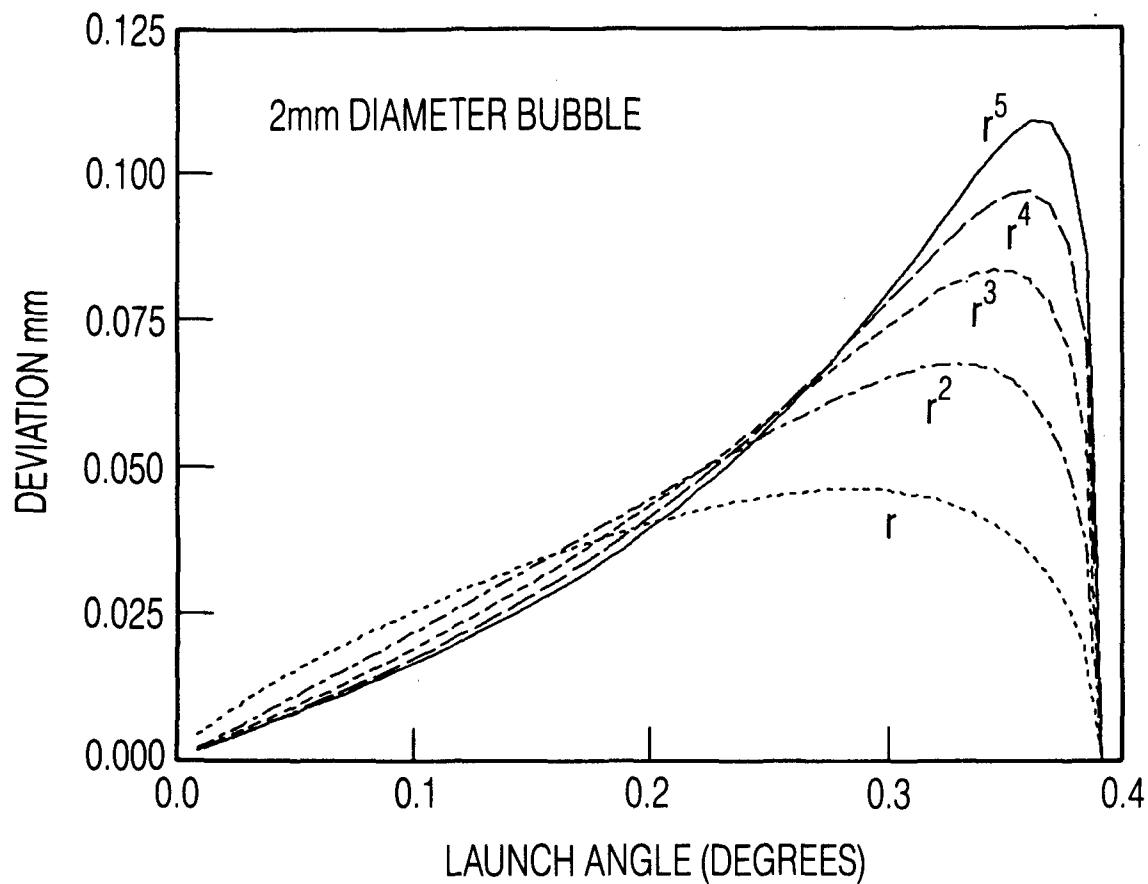
Fig. 22. Deviation at the Detector Ring of a Ray Passing Through a 2 mm Turbulence Bubble with a Cylindrically Symmetric Variation in Density for Five Different Density Gradients. The edge density is a factor of 2 greater than the center density.
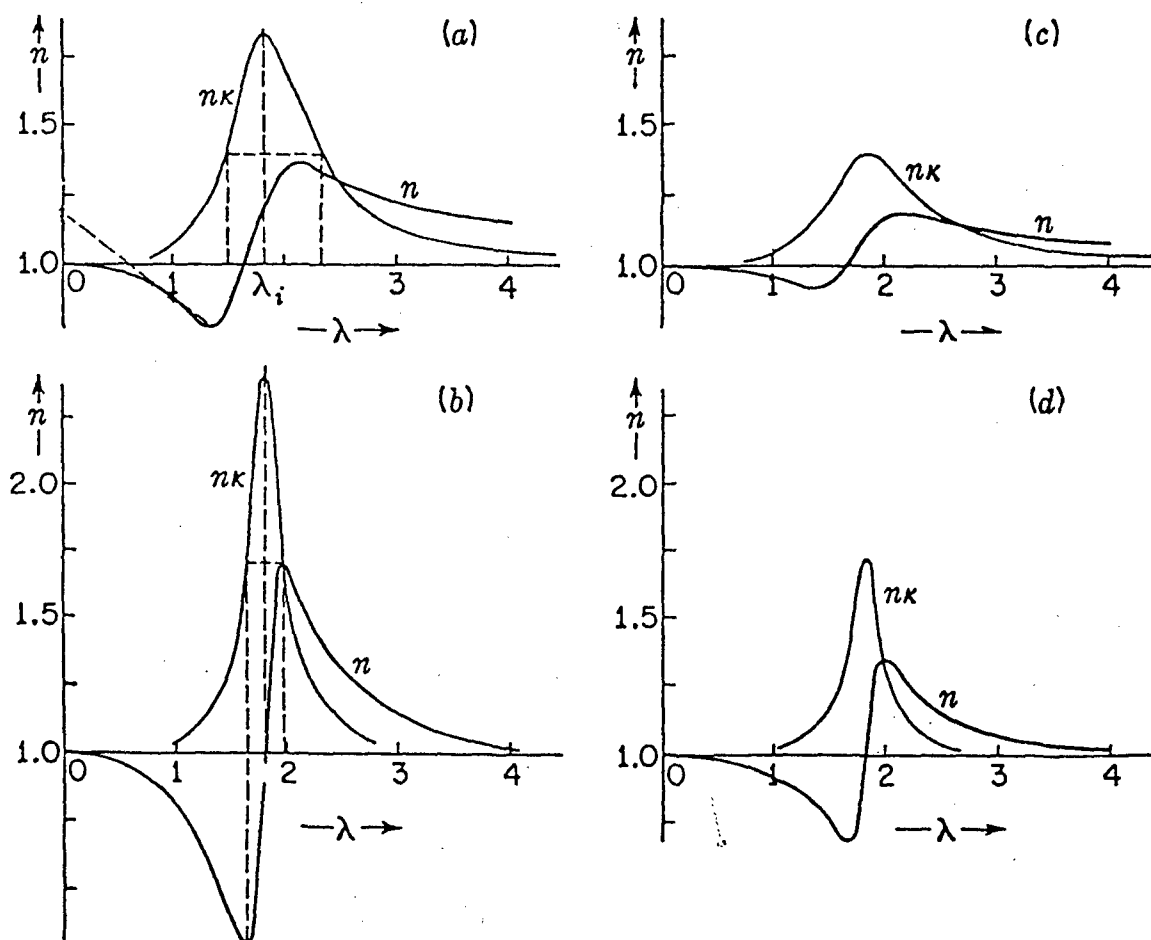
Fig. 23. Ideal Dispersion Curves for an Absorption with Different Amounts of Damping and Absorption. (a) Strong absorption, strong damping; (b) strong absorption, weak damping; (c) weak absorption, strong damping; (d) weak absorption, weak damping. The absorption coefficient is κ.

with a bandwidth much less than the absorption linewidth centered on the peak absorption. Any drift in wavelength, however, could cause appreciable refraction if the probe gas is a major species. This is not expected to be a problem if the concentration of the species is less than 0.1%

V. DATA REDUCTION: LINEARITY, DYNAMIC RANGE, AND ERROR

A. INTRODUCTION

In this section, we consider the inference of the concentration and temperature from fan beam projection data. As introduced in Section I, the projection data are defined by

$$P(r,\theta) = - \ln [I(r,\theta)/I_o] = - \ln R \tag{78}$$

and are related to the flow cross-sectional map $F(x,y)$

$$P(r,\theta) = \int_o^L F(x,y)d\ell \tag{79}$$

where

$$F(x,y) = q(\nu_o)n_J(x,y) \tag{80}$$

where $q(\nu)$ is the absorption cross section, n_J is the number of molecules in rotational level J of the molecule under investigation, and R is the ratio of intensities. The concentrations n_o and n_J are related via the Boltzmann factor when the gas is in thermodynamic equilibrium

$$n_J = n_o \frac{g_J \exp(-E/kT)}{Q(T)} \tag{81}$$

where g_J is the statistical weight of energy level E_J and Q(T) is the partition function. The rotational energy level diagram of a typical diatomic molecule (N_2, CO) is shown in Fig. 24. To the left of the energy levels is a scaled plot of the Boltzmann factor [Eq. (81)], indicating the relative distribution of n_o among the various levels for three temperatures.

If the flow is sampled at two different optical frequencies ν_1 and ν_2, with corresponding absorptions originating from levels J_1 and J_2, with cross sections q_1 and q_2, then two field functions $F_1(x,y)$ and $F_2(x,y)$ can be obtained by reconstruction from the projection data
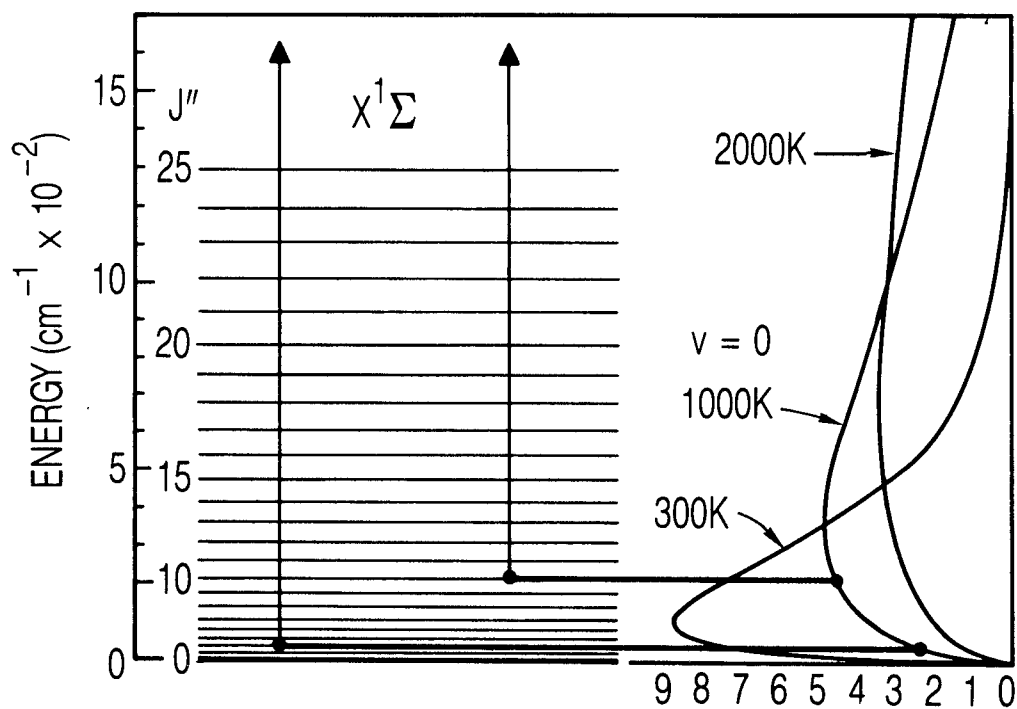
Fig. 24   Energy Level Diagram of $^1\Sigma$ Ground Electronic and Vibrational State of a Typical Diatomic Molecule. The relative population in the rotational levels are shown by the Boltzmann curves to the left for three temperatures.

$P_1(\nu_1)$ and $P_2(\nu_2)$. Substituting Eq. (81) into Eq. (80), writing this expression separately for each absorption at ν_1 and ν_2, we can solve the resulting two equations simultaneously to obtain expressions for temperature and concentration maps

$$T(x,y) = \frac{(E_{J_1} - E_{J_2})}{k \ln\left(\dfrac{F_2(x,y)}{F_1(x,y)} \dfrac{q_1(\nu_1)}{q_2(\nu_2)} \dfrac{g_{J_1}}{g_{J_2}}\right)} \qquad (82)$$

$$n_o(x,y) = \frac{F_1(x,y)Q(T)}{q_1(\nu_1)g_{J_1}} \exp\left[E_{J_1}/kT(x,y)\right] \qquad (83)$$

Equations (82) and (83) form the basis of our analysis.

B. LINEARITY AND DYNAMIC RANGE

We first consider the dynamic range over which measurements of temperature and concentration can be made, given a linear range over which the ratio R can be measured. The linear range of the detector system determines the linear range of R. The detector system consists of a fast photodiode, the sampling electronics, and the analaog-to-digital (A/D) converter. Photodiodes operating as photoconductors are linear over a minimum of seven decades. Fast sampling electronics can be obtained that are linear over four decades. Thus, a 10 or 12 bit A/D will limit the linear dynamic range of R to 10^3 or 4×10^3, respectively.

To find the dynamic range of $n_o(x,y)$ for a given dynamic range in R, we note

$$\Delta n_o = \int_{R_1}^{R_2} \frac{\partial n_o}{\partial F} \frac{\partial F}{\partial R} \, dR \qquad (84)$$

67

From Eqs. (78) and (79)

$$\int F \, d\ell = - \ln R$$

Taking the derivative of this equation with respect to R and interchanging the order of integration and differentiation on the left side, we have

$$\int \frac{\partial F}{\partial R} \, d\ell = - \frac{1}{R}$$

or

$$\frac{\partial F}{\partial R} = - \frac{d}{d\ell} \left(\frac{1}{R} \right)$$

$$= \frac{1}{R^2} \frac{dR}{d\ell}$$

Noting

$$\frac{dR}{d\ell} = \frac{d}{d\ell} \, e^{-n_J q \ell} = - n_J q R$$

we find

$$\frac{\partial F}{\partial R} = \frac{-n_J q}{R} \qquad (85)$$

Taking the derivative of Eq. (83) with respect to F, substituting this result and Eq. (85) into Eq. (84), and using Eq. (81) for n_J, we find, on integration

$$\frac{\Delta n(x,y)}{n_o(x,y)} = - \ln \left(R_2 / R_1 \right) \qquad (86)$$

$$= 8.3 \ (12 \text{ bit resolution})$$

68

which is the fractional dynamic range for a given pixel. Equation (86) is the same result one obtains for simple absorption experiments. This dynamic range can be extended by an order of magnitude by viewing two different spectral lines simultaneously. It is not difficult to find two absorption lines with vastly different peak absorptions within a relatively narrow spectral range [see transitions listed for $F_1(1.5)$ in Table 4, for example].

Similarly, the dynamic range in temperature can be estimated from

$$\Delta T = \int_{R_{T_a}}^{R_{T_b}} \frac{\partial T}{\partial F_1} \frac{\partial F_1}{\partial R_1} dR_1 + \int_{R_{T_a}}^{R_{T_b}} \frac{\partial T}{\partial F_2} \frac{\partial F_2}{\partial R_2} dR_2 \tag{87}$$

Using Eqs. (80), (82), and (85), we find

$$\Delta T = \frac{(E_{J_1} - E_{J_2})}{k} \ln\left[\frac{g_{J_1}}{g_{J_2}} \frac{n_{J_2}}{n_{J_1}}\right]^{-2} \left[\ln\left(\frac{R_{T_b}}{R_{T_a}}\right)_{J_1} - \ln\left(\frac{R_{T_b}}{R_{T_a}}\right)_{J_2}\right] \tag{88}$$

C. ERROR

In this subsection, we consider noise in the reconstructed image and the propagation of this error to the concentration and temperature. Tomography has a considerably higher sensitivity than single ray absorption due to the averaging effect of the many views (projections). Bennett and Byer (Ref. 43) have studied the noise in the reconstructed image for fan beam geometry using a convolution back projection algorithm that utilized the sampled Ramachandran-Lakshminarayanan (RL) kernel. When the noise in each projection is uncorrelated with the noise in any other projection (but allowing for correlation within a given projection), the reconstructed noise variance is

69

$$\sigma_F^2(\rho) = \sigma_P^2 \left[\frac{\pi^2 - 3}{18 N_f a^2 R_D^2} \right] w(\rho) \tag{89}$$

where

$$w(\rho) = \frac{1 + \rho^2/2}{(1 - \rho^3)^3} \tag{90}$$

where σ_p is the variance of the projection data, ρ is the distance from the center of the source-detector ring to the reconstructed pixel divided by the radius of the source-detector ring R_D, and a is the angular separation between the detectors. Hence, the uncertainty in a given pixel in the reconstructed field is less than that in the projection data by the square root of the bracketed term in Eq. (89). Note that the noise is geometry dependent through the term $w(\rho)$. Thus, keeping F ($= R_D/r$) as large as possible minimizes the "geometrical" noise.

Reference 43 defines the equivalent noise absorption across a pixel as $e^{-\delta_{min}}$, where

δ_{min} = (rms noise amplitude) × (normalized resolution for the RL kernel)

$$\tag{91}$$

$$= \sigma_f \times a$$

Now, consider the two-frequency case, where both temperature and concentration are measured simultaneously. Given the variances σ_u^2 and σ_v^2 of the two measured parameters u and v, the variance σ_x of the desired parameter x can be estimated using (Ref. 44)

$$\sigma_x^2 \approx \sigma_u^2 \left(\frac{\partial x}{\partial u} \right)^2 + \sigma_v^2 \left(\frac{\partial x}{\partial v} \right)^2 + 2\sigma_{uv} \left(\frac{\partial x}{\partial u} \right) \left(\frac{\partial x}{\partial v} \right) \tag{92}$$

where σ_{uv} is the covariance. If we assume that the fluctuations in R_1 and R_2 are uncorrelated, the covariance will average to zero and the temperature variance is

$$\sigma_T^2 = \sigma_{F_1}^2 \left(\frac{\partial T}{\partial F_1}\right)^2 + \sigma_{F_2}^2 \left(\frac{\partial T}{\partial F_2}\right)^2$$

$$= \sigma_F^2 \left[\left(\frac{\partial T}{\partial F_1}\right)^2 + \left(\frac{\partial T}{\partial F_2}\right)^2\right] \tag{93}$$

Calculating the derivatives from Eq. (82), we find

$$\sigma_T = \sigma_F \frac{\left(E_{J_1} - E_{J_2}\right)}{k} \left[\ln\left(\frac{g_{J_1} n_2}{g_{J_2} n_1}\right)\right]^{-2} \left(\frac{1}{F_1^2} - \frac{1}{F_2^2}\right)^{1/2} \tag{94}$$

Similarly

$$\sigma_{n_o}^2 = \sigma_{F_1}^2 \left(\frac{\partial n_o}{\partial F_1}\right)^2 + \sigma_T^2 \left(\frac{\partial n_o}{\partial T}\right)^2 + \sigma_F \sigma_T \left(\frac{\partial n_o}{\partial F_1}\right)\left(\frac{\partial n_o}{\partial T}\right) \tag{95}$$

assuming that σ_{FT} is no greater than $\sigma_{F_1} \sigma_T$. Calculating the derivative of n_o, we find

$$\sigma_{n_o} = \left(\frac{\exp(E_J/kT)}{q_1 g_{J_1}}\right) \left[\sigma_F^2 Q^2 + \sigma_T^2 F_1^2 \left(\frac{\partial Q}{\partial T} - \frac{Q E_J}{kT^2}\right)^2 \right.$$
$$\left. + \sigma_T \sigma_F Q F_1 \left(\frac{\partial Q}{\partial T} - \frac{Q E_J}{kT^2}\right)\right]^{1/2} \tag{96}$$

D. EXAMPLE

In this subsection, the dynamic range and error expressions are evaluated for the OH molecule and the geometry discussed in the previous subsections. The hydroxyl radical is an important minor species in hydrocarbon combustion. Absolute transition probabilities are available for all

71

electronic transitions in the (0,0) band of the $X^2\Pi_{3/2,1/2} - A^2\Sigma$ system (Ref. 45). The absorption lines from this band appear near 3100 Å, a spectral region accessible by a doubled dye laser. In this spectral region, ultraviolet (UV) fiber optics can transmit enough power to saturate the detection system. Within the power handling capability of the fibers, the range of concentrations that can be measured for a given species can be changed by changing the laser power into the instrument and adjusting an attenuating filter in the I_o reference channel to keep the range centered. Thus, the 12 bit dynamic range in R can be maintained for values of R that may cover several orders of magnitude. The range of concentration can also be adjusted by the choice of spectral line. The absorption cross sections of most molecules vary one to two orders of magnitude within the spectral range of a single laser dye. This is certainly true for OH.

The structure of the ground state of OH is a spin split doublet with a splitting constant of A_v = 139.21 - 0.275v (Ref. 46). The structure is not well described as either Hunds case (a) or case (b) coupling, and intermediate coupling formulas should be used to calculate the structure. The splitting is inverted with the $^2\Pi_{1/2}$ (F_2) state lying above the $^2\Pi_{3/2}$ (F_1) state. There are 12 rotational branches of electric-dipole-allowed transitions between the ground state and the $A^2\Sigma$ state.

The energies of the first 10 rotational levels of both spin states are given in Table 4. The fractional population of each of these levels is calculated at a temperature of 1000 K using Eq. (81). The partition function for this molecule can be approximated by (Refs. 46, 47)

$$Q(T) = (2S + 1)(2 - \delta_{0\Lambda})\left(1 + e^{-hc\omega_e/kT}\right)\left(\frac{kT}{hcB_e}\right) \tag{97}$$

$$= 148 \text{ at } 1000 \text{ K for OH}$$

where S = 1/2 and Λ = 1. The derivative of Q(T) is needed for Eq. (96)

Table 4. Selected Properties of OH[a]

$^2\Pi_{1/2}$ (F$_2$)

J"	$F_2(cm^{-1})$	$f(10^{-2})$*	$^{\Delta N}\Delta J_{J'J"}(J")$	$A_{J'J"}(sec^{-1})$	$\lambda(Å)$	$q_{eff}(cm^2)$
0.5	126.5	1.13				
1.5	187.5	2.06	$^OP_{12}(1.5)$	7.36×10^4	3106	6.0×10^{-16}
→ 2.5	288.8	2.68	$^PP_{22}(1.5)$	3.85×10^5	3100	3.1×10^{-15}
3.5	429.4	2.92				
4.5	608	2.82				
5.5	824	2.48	$^QQ_{22}(5.5)$	6.25×10^5	3093	2.5×10^{-15}
6.5	1078	2.01	$^QR_{22}(5.5)$	4.6×10^4	3093	1.6×10^{-16}
→ 7.5	1368	1.52	$^PQ_{12}(5.5)$	7.99×10^4	3112	3.3×10^{-16}
8.5	1693	1.07				
9.5	2054	0.704				
10.5	2453	0.436	$^QQ_{22}(10.5)$	6.22×10^5	3106	2.5×10^{-15}

$^2\Pi_{3/2}$ (F$_1$)

J"	$F_1(cm^{-1})$	$f(10^{-2})^b$	$^{\Delta N}\Delta J_{J'J"}(J")$	$A_{J'J"}(sec^{-1})$	$\lambda(Å)$	$q_{eff}(cm^2)$
→ 1.5	0.0	2.71	$^PP_{11}(1.5)$	8.6×10^5	3082	6.9×10^{-15}
2.5	83.9	3.60	$^RQ_{21}(1.5)$	1.8×10^5	3072	7.2×10^{-16}
3.5	201.9	4.05	$^RR_{11}(1.5)$	8.1×10^4	3072	2.1×10^{-16}
4.5	355.1	4.06				
5.5	543.0	3.72				
6.5	767.5	3.14				
→ 7.5	1029	2.46	$^QP_{21}(7.5)$	4.66×10^4	3090	2.1×10^{-16}
8.5	1324	1.81	$^RR_{11}(7.5)$	2.6×10^5	3064	9.2×10^{-16}
9.5	1655	1.25				
10.5	2019	0.81	$^QQ_{11}(10.5)$	6.2×10^5	3099	2.5×10^{15}

[a]Energies and A values from Reference 45.

[b]Fractional populations calculated for a temperature of 1000 K.

$$\frac{dQ(T)}{dT} = \frac{(2S + 1)(2 - \delta_{0\Lambda})k}{hcB} \left[1 + \exp(-hc\omega_e/kT)\left(1 + \frac{hc\omega_e}{kT}\right)\right] \quad (98)$$

$$= 0.15 \text{ at } 1000 \text{ K for OH}$$

The absorption cross sections in Table 4 were calculated from the Einstein A coefficients using (Ref. 49)

$$\int q(\nu)d\nu = \left(\frac{g_{J_2}}{g_{J_1}}\right) \frac{\lambda^2}{8\pi} A_{J_2 J_1} \quad (99)$$

To evaluate Eq. (99) for a value of the cross section, we must assume a form for the lineshape. If q_o is the cross section at the line center ν_o, and $G(\nu)$ is the lineshape function, then

$$q(\nu) = q_o G(\nu)$$

For a Doppler (inhomogeneously) broadened line, $G(\nu)$ is Gaussian, i.e.

$$G_D(\nu) = \exp\left[(\nu - \nu_o)^2/\gamma_D^2\right]$$

where $G_D(\nu_o) = 1$, $\int G_D(\nu)d\nu = \frac{\gamma_D}{\sqrt{\pi}}$, and γ_G is the e^{-1} halfwidth. For a pressure (homogeneously) broadened line, $G(\nu)$ is Lorentzian, i.e.

$$G_D(\nu) = \gamma_P^2\left[(\nu - \nu_o)^2 + \gamma_P^2\right]^{-1}$$

where $G_P(\nu_o) = 1$, $\int G_P(\nu)d\nu = \pi\gamma_P$, and γ_P is the half width at half maximum (HWHM). Note that $\gamma_D = \gamma_P/\sqrt{\ln 2}$. An OH molecule in a combustion environment has absorption lines that are primarily pressure broadened, so

$$q_o = \frac{\lambda^2}{8\pi^2} \frac{g_{J_2}}{g_{J_1}} \frac{A_{J_2 J_1}}{\gamma_P} \quad (100)$$

For laser radiation with a finite bandwidth centered at ν_o, the peak cross section is not realized for all the laser radiation, and an effective (so-called midband) cross section equal to $0.5\ q_o$ is used. The values of this

74

cross section are listed in Table 4. The values for A in Table 4 were taken from Reference 45. The linewidths are functions of T, J, and the collision environment. An average value of 0.05 cm^{-1} was adopted for the halfwidth (Ref. 50).

We consider first an experiment using a single absorption line. For this situation, only $n_J(T)$ can be measured for each pixel, and the relative number density cannot be measured unless either $T(x,y)$ = constant or n_J is not a function of temperature. The first case is physically uninteresting. Fortunately, the second case is possible because most molecules (that are amenable to this technique) have a level from which a spectrally accessible line originates whose population is relatively insensitive to changes in T. For example, the absorption from any line originating from the E_J = 0 energy level is a function of temperature only through the partition function. The partition function to first approximation is a linear function of T [Eq. (97)], and a 200 K variation in T introduces a 20% uncertainty in the inferred values of the concentration for temperatures near 1000 K. In Table 4, the $^PP_{11}(1.5)$ and $^RR_{11}(1.5)$ both originate from this level and have absorption cross sections that differ by nearly two orders of magnitude, allowing both high and low concentration environments to be studied. The dynamic range, however, is still limited by Eq. (86). For a given temperature range, higher accuracy may be attainable by choosing a rotational level where the variation in the partition function due to temperature is offset by the change resulting from the exponential function [Eq. (83)].

Using Eq. (91), the noise level in the density measurement can be estimated. If we assume that the ratio of intensities R (= I/I_0) can be measured with 10 bit accuracy, the relative error

$$e_R \equiv \frac{\sigma_R}{R} \tag{101}$$

is 0.1%. From Eqs. (78) and (92), the projection variance is

$$\sigma_P = \sigma_R \frac{\partial P}{\partial R} = \frac{\sigma_R}{R} = e_R \qquad (102)$$

The projection error is related to the error in the field function error through Eq. (89). We consider our optimum geometry for a 4 in. diameter flow (r = 5 cm) to have n_f = 96, F = 3.86, and choose an average r/2 = 2.5 cm to obtain a value for ρ of 0.1275. Then, from Eq. (90), w = 1.01 and $\sigma_F = 0.31 \sigma_P$. Allowing

$$\delta_{min} = n_{noise} q \ell_{res} = n_{noise} q R_D a$$

we have, from Eq. (93)

$$n_{noise} = \frac{\sigma_F}{q R_D} \qquad (103)$$

For the $^P P_{11}$ (1.5) line, n_{noise} = 2 × 10^9 cm^{-3} = 7 × 10^{-11} Amagat. For a 4 in. flow diameter, the maximum detectable density is 10^{14} cm^{-3} for an attenuation of ~ 10^4. Because of limited dynamic range, the minimum detectable intensity is ~ 10^{13}. Thus, this noise level is ~ 0.02% of this lower level, a value considerably below other sources of noise, such as laser speckle.

The more important experiment is the probing of two different spectral lines of a single species. By the proper choice of lines, the dynamic range of concentration can be increased by nearly an order of magnitude, and a spatial map of the temperature also can be recovered. To increase the dynamic range of n_o, two lines with an absorption cross section that differ by a factor of ~ 10 should be chosen. According to Eq. (88), the dynamic range of T varies directly with the energy difference between the lower levels of the two lines. From Eq. (94), this is also true for σ_T. Because the dynamic range is large for T, closely spaced levels should be selected. The dynamic range of T can be increased by choosing lines that originate from opposite sides of the peak of the Boltzmann curve so that the two logarithmic terms in the last bracket of Eq. (88) add. Finally,

note that the number density can be calculated from either R_1 or R_2. The variance of n_0 is decreased by choosing an absorption from an energy with a low value of $\exp(E_J/kT)/g_J$ and with a large absorption cross section. With these criteria in mind, we select the ${}^P P_{22}$ (1.5) and ${}^P Q_{12}$ (5.5) lines.

Equation (88) is evaluated to obtain the dynamic range in T assuming that the range of the ratios for the J_2 line may take the full 12 bit range, but the range of ratios for J_1 is a factor of 10 less. Accordingly, we find $\Delta T = 7850$ K. The dynamic range of n_0 is $\ln(4 \times 10^3) \times \{q[{}^P P_{22}(1.5)]/q[{}^P Q_{12}(5.5)]\} \approx 78$. The variance in temperature is given by Eq. (94). Noting $F = qn$, and evaluating for a partial density of 10^{-4} Amagat, we find $\sigma_T = 7.6$ for $e_R = 0.1\%$. Finally, evaluating Eq. (92) for the above conditions, we find $\sigma_{n_0} = 2 \times 10^{13} = 8 \times 10^{-7}$ Amagat--an accuracy of 0.8%.

REFERENCES

1. D. R., Ballal, A. J. Lightman, and P. P. Yaney, "Development of Test Facility and Optical Instrumentation for Turbulent Combustion Research," J. Propulsion 3, 97 (1987).

2. M. B. Long, D. C. Fourguette, M. C. Escoda, and C. B. Layne, "Instantaneous Ramanography of a Turbulent Diffusion Flame," Opt. Lett. 8, 244 (1983).

3. L.-R. Socket and M. Lucquin, "Use of Multichannel Pulsed Raman Spectroscopy as a Diagnostic Technique in Flames," Combust. Flame 36, 109 (1979).

4. B. F. Webber, M. B. Cong, and R. K. Chang, Two Dimensional Average Concentration Measurements in a Jet Flow by Raman Scattering," Appl. Phys. Lett. 35, 119 (1979).

5. P. C. Black and R. K. Chang, "Laser-Raman Multichannel Analyzer for Transient Gas Concentration Profile and Temperature Determination," AIAA J. 16, 295 (1978).

6. M. B. Long, B. F. Weber, and R. K. Chang, "Instantaneous Two-Dimensional Concentration Measurements in a Jet Flow by Mie Scattering," Appl. Phys. Lett, 34, 22 (1979).

7. M. B. Long, B. T. Chu, and R. K. Chang, "Instantaneous Two-Dimensional Gas Concentration Measurements by Light Scattering," AIAA J. 19, 1151 (1981).

8. M. Winter, J. K. Lam, and M. B. Long, "Techniques for High-Speed Digital Imaging of Gas Concentrations in Turbulent Flows," Exp. Fluids 5, 177 (1987).

9. B. Yip, J. K. Lam, M. Winter, and M. B. Long, Science 235, 1209 (1987).

10. B. Yip, R. L. Schmitt, and M. B. Long, "Instantaneous Three-Dimensional Concentration Measurements in Turbulent Jets and Flows," Opt. Lett. 13, 96 (1988).

11. M. G. Allen and R. K. Hanson, "Planar Laser-Induced-Fluorescence Monitoring of OH in a Spray Flame," Opt. Eng. 25, 1309 (1986).

12. G. Kychakoff, R. D. Howe, and R. K. Hanson, "Quantitative Flow Visualization Technique for Measurements in Combustion Gases," Appl. Opt, 23, 704 (1984).

REFERENCES (Continued)

13. J. Haumann, J. M. Seitzman, and R. K. Hanson, "Two-Photon Digital Imaging of CO in Combustion Flows Using Planar Laser-Induced Fluorescence," Opt. Lett. 11, 776 (1986).

14. J. M. Seitzman, J. Haumann, and R. K. Hanson, "Quantitative Two-Photon LIF Imaging of Carbon Monoxide in Combustion Gases," Appl. Opt. 26, 2892 (1987).

15. G. Kychakoff, P. H. Paul, I. van Cruyningen, and R. K. Hanson, "Movies and 3-D Images of Flowfields Using Planar Laser-Induced Fluorescence," Appl. Opt. 26, 2498 (1987).

16. J. S. Bendat and A. G. Piersol, Random Data: Analysis and Measurement Procedures, Wiley Interscience, New York (1971).

17. J. A. L. Thomson, A. R. Davis, and K. G. P. Sulzmann, "Conceptual Design of an Airborne Laser Doppler Velocimeter," PD-B-76-118, Physics Dynamics, Inc., Berkeley, California (1976).

18. G. N. Ramachandran and A. V. Lakskmenarayanan, "Three Dimensional Reconstruction from Radiographs and Electron Micrographs: Application of Convolutions Instead of Fourier Transforms," Proc. Natl. Acad. Sci. U. S. 68, 2236 (1971).

19. K. Gordon, R. Bender, and G. T. Herman, "Algebraic Reconstruction Techniques for Three-Dimensional Electron Microscopy and X-ray Photography," J. Theor. Biol. 29, 471 (1970).

20. R. Goulard and P. J. Emmerman, "Combustion Diagnostics by Multiangular Absorption," Topics in Current Physics, 20; Inverse Scattering Problems in Optics, H. P. Baltes, ed., Springer-Verlag, New York (1980).

21. R. Goulard and S. R. Ray, "Optical Tomography in Combustion," Advances in Remote Sensing Retrieval Methods, A. Deepak, H. E. Fleming, and M. T. Chahine, eds., A. Deepak Publishing (1985).

22. S. R. Ray and H. G. Semerjian, "Laser Tomography for Simultaneous Concentration and Temperature Measurement in Reacting Flows," Paper 83-1553, AIAA 18th Thermophysics Conference, Montreal, Canada (1983).

23. K. E. Bennett, G. W. Faris, and R. L. Byer, "Experimental Optical Fan Beam Tomography," Appl. Opt. 2223, 2678 (1984).

24. K. Bennett and R. L. Byer, "Optical Tomography: Experimental Verification of Noise Theory," Opt. Lett. 9, 270 (1984).

25. G. W. Faris and R. L. Byer, "Quantitative Optical Tomographic Imaging of a Supersonic Jet," Opt. Lett 7, 413 (1986).

26. R. Synder and L. Hesselink, "High Speed Optical Tomography," Appl. Opt. 24, 4046 (1985).

27. G. W. Faris and R. L. Byer, "Beam Deflection Optical Tomography," Opt. Lett. 12, 72 (1987).

28. G. W. Faris and R. L. Byer, "Beam Deflection Optical Tomography of a Flame," Opt. Lett. 12, 155 (1987).

29. G. W. Faris and R. L. Byer, "Quantitative Three-Dimensional Optical Tomographic Imaging of Supersonic Flows," Science 238, 1700 (1987).

30. G. W. Faris and R. L. Byer, "Beam Deflection Optical Tomography Facilitates Flow Analysis," Laser Focus, 145 (1987).

31. H. M. Hertz, "Experimental Determination of 2-D Flame Temperature Fields by Interferometric Tomography," Opt. Commun. 54, 131 (1985).

32. R. Synder and L. Hesselink, "Optical Tomography for Flow Visualization of the Density Field Around a Revolving Helicopter Rotor Blade," Appl. Opt. 23, 3650 (1984).

33. D. Modarress and H. Tan, "Application of Tomography in 3-D Transonic Flows, AIAA-87-1374, AIAA 19th Fluid Dynamics, Plasma Dynamics and Laser Conference, Honolulu, Hawaii (1987).

34. R. Synder and L. Hesselink, "Measurement of Mixing Fluid Flows with Optical Tomography," Opt. Lett. 13, 87 (1988).

35. H. M. Hertz and G. W. Faris, "Emission Tomography of Flame Radicals," Opt. Lett. 13, 351 (1988).

36. M. Hino, T. Aono, M. Nakajima, and S. Yuta, "Light Emission Computed Tomography System for Plasma Diagnostics," Appl. Opt. 26, 4742 (1987).

37. L. Hesselink, "Digital Image Processing in Flow Visualization," Ann. Rev. Fluid Mech. 20, 421 (1988).

38. L. Hesselink, "Optical Tomography," Handbook of Flow Visualization, Washington, D.C., Hemisphere (1987).

REFERENCES (Continued)

39. Appl. Opt. 24 (23) (1985).

40. J. O. Hinze, Turbulence, 2nd ed., McGraw-Hill Book Co., New York (1975), p. 8.

41. E. Hecht and A. Zajac, Optics, Addison-Wesley, Reading, Mass. (1974).

42. D. Marcuse, Light Transmission Optics, Van Nostrand Reinhold Co., New York (1982).

43. K. E. Bennett and R. L. Byer, "Fan-Beam-Tomography Noise Theory," J. Opt. Soc. Am. A 3, 624 (1986).

44. P. R. Bevington, Data Reduction and Error Analysis for the Physical Sciences, McGraw Hill, New York (1969).

45. A. Goldman and J. R. Gillis, "Spectral Line Parameters for the $A^2\Sigma$-$X^2\Pi$(0,0) Band of OH for Atmospheric and High Temperatures," J. Quant. Spectro. Radiat. Transfer 25, 111 (1981).

46. K. P. Huber and G. Herzberg, Molecular Spectra and Molecular Structure IV. Constants of Diatomic Molecules, Van Nostrand Reinhold Co., New York (1979).

47. J. B. Tatum, "The Interpretation of Intensities in Diatomic Molecular Spectra," Ap. J. Supple. Series 124, Vol XVI, 21 (1967).

48. G. Herzberg, Spectra of Diatomic Molecules, Van Nostrand Reinhold Co., New York (1950).

49. A. P. Thorne, Spectrophysics, Chapman and Hall, London (1974).

50. C. C. Wang, D. K. Killinger, and C.-M. Huang, "Rotational Dependence in the Linewidth of the Ultraviolet Transitions of OH," Phys. Rev. A 22, 188 (1980).